

- 1 - Luo et al.: Multi-layer Arctic Mixed-Phase Clouds Simulated by a CRM

1 **Multi-Layer Arctic Mixed-Phase Clouds Simulated by a**
2 **Cloud-Resolving Model: Comparison with ARM Observations**
3 **and Sensitivity Experiments**

4
5
6 Yali Luo ¹, Kuan-Man Xu ², Hugh Morrison³, Greg M. McFarquhar⁴,
7 Zhien Wang⁵, and Gong Zhang⁴

8
9 ¹ State Key Laboratory of Severe Weather, Chinese Academy of Meteorological
10 Sciences, Beijing, China

11 ² NASA Langley Research Center, Hampton, VA, USA

12 ³ National Center for Atmospheric Research, Boulder, CO, USA

13 ⁴ University of Illinois at Urbana-Champaign, Urbana, IL, USA

14 ⁵ University of Wyoming, Laramie, WY, USA

15
16
17 November 2, 2007

18
19
20 Submitted to *Journal of Geophysical Research*

21
22
23 Corresponding author: Dr. Yali Luo

24 State Key Laboratory of Severe Weather

25 Chinese Academy of Meteorological Sciences

26 Beijing 100081, China

27 E-mail: yali@cams.cma.gov.cn

28

28

ABSTRACT

29 A cloud-resolving model (CRM) is used to simulate the multiple-layer mixed-phase
30 stratiform (MPS) clouds that occurred during a three-and-a-half day subperiod of the
31 Department of Energy-Atmospheric Radiation Measurement Program's Mixed-Phase
32 Arctic Cloud Experiment (M-PACE). The CRM is implemented with an advanced two-
33 moment microphysics scheme, a state-of-the-art radiative transfer scheme, and a
34 complicated third-order turbulence closure. Concurrent meteorological, aerosol, and ice
35 nucleus measurements are used to initialize the CRM. The CRM is prescribed by time-
36 varying large-scale advective tendencies of temperature and moisture and surface
37 turbulent fluxes of sensible and latent heat.

38 The CRM reproduces the occurrences of the single- and double-layer MPS clouds
39 as revealed by the M-PACE observations. However, the simulated first cloud layer is
40 lower and the second cloud layer thicker compared to observations. The magnitude of the
41 simulated liquid water path agrees with that observed, but its temporal variation is more
42 pronounced than that observed. As in an earlier study of single-layer cloud, the CRM also
43 captures the major characteristics in the vertical distributions and temporal variations of
44 liquid water content (LWC), total ice water content (IWC), droplet number concentration
45 and ice crystal number concentration (n_{is}) as suggested by the aircraft observations.
46 However, the simulated mean values differ significantly from the observed. The
47 magnitude of n_{is} is especially underestimated by one order of magnitude.

48 Sensitivity experiments suggest that the lower cloud layer is closely related to the
49 surface fluxes of sensible and latent heat; the upper cloud layer is probably initialized by
50 the large-scale advective cooling/moistening and maintained through the strong longwave
51 (LW) radiative cooling near the cloud top which enhances the dynamical circulation;
52 artificially turning off all ice-phase microphysical processes results in an increase in LWP
53 by a factor of 3 due to interactions between the excessive LW radiative cooling and extra
54 cloud water; heating caused by phase change of hydrometeors could affect the LWC and

55 cloud top height by partially canceling out the LW radiative cooling. It is further shown
56 that the resolved dynamical circulation appears to contribute more greatly to the
57 evolution of the MPS cloud layers than the parameterized subgrid-scale circulation.

58 **1. Introduction**

59 Arctic clouds have been identified as playing a central role in the Arctic
60 climate system that has been changed significantly in the recent decades (ACIA,
61 2005) and can potentially impact global climate (Curry et al., 1996; Vavrus, 2004). A
62 few field campaigns have been conducted to improve the understanding of cloud-
63 radiative interactions in the Arctic: the Beaufort Arctic Sea Experiment (BASE;
64 Curry et al., 1997), the First International Satellite Cloud Climatology Project (ISCCP)
65 Regional Experiment (FIRE) - Arctic Cloud Experiment (ACE; Curry et al., 2000),
66 the Surface Heat Budget of the Arctic (SHEBA; Uttal et al., 2002), and the
67 Department of Energy (DOE) Atmospheric Radiation Measurement (ARM)
68 Program's Mixed-Phase Arctic Cloud Experiment (M-PACE; Harrington and
69 Verlinde, 2004; Verlinde et al., 2007). These field campaigns identified that mixed-
70 phase stratiform (MPS) clouds were prevalent in Arctic transition seasons (Intrieri et
71 al., 2002; Verlinde et al., 2007), especially during the fall over Barrow at the ARM
72 North Slope of Alaska (NSA) site (Wang et al., 2005; Shupe et al., 2005). This type
73 of mixed-phase cloud is a water-dominated cloud layer with precipitating ice, yet they
74 persist for long periods of time (Hobbs and Rangno, 1998; McFarquhar et al., 2007).

75 Previous observational analysis and modeling studies revealed that large-scale
76 advection, surface flux, microphysics, and radiation could affect the formation and
77 evolution of mixed-phase Arctic clouds. Observations from 12 research flights during
78 BASE suggested local interactions between the clouds and the underlying surface
79 (Curry et al., 1997). Curry et al.'s analysis also suggested that large-scale advection
80 and leads (areas of open water between ice floes) appear to play a role in forming and
81 maintaining the cloud systems. Utilizing aircraft measurements from the BASE
82 experiment and the National Center of Environmental Prediction (NCEP) reanalysis,
83 Pinto (1998) suggested the importance of large-scale moisture and temperature
84 advection and cloud-top radiative cooling for the evolution of these clouds. In

85 addition, Pinto speculated the importance of ice forming nuclei (IFN) to cloud
86 stability. In Harrington et al. (1999), the soundings from a summer case were
87 consistently cooled in cloud-resolving model (CRM) simulations to produce
88 physically plausible mixed-phase situations, because of lack of soundings for mixed-
89 phase Arctic low clouds at that time. The temperature, ice concentration, and the habit
90 of the ice crystals were found to affect the stability of the simulated mixed-phase
91 cloud layer. In particular, cloud layer stability was shown to be most strongly
92 dependent upon the concentration of IFN. It was also shown that ice production and
93 sedimentation could assist the formation of a second, lower cloud layer. Harrington
94 and Olsson (2001) illustrated that IFN concentration could significantly impact
95 evolution of the simulated mixed-phase clouds that occurred in an environment with a
96 strong surface heat flux. Moreover, ice formation has been examined in a few
97 modeling studies (e.g., Jiang et al., 2000; Morrison and Pinto, 2005; Prenni et al.,
98 2007; Fridlind et al., 2007), as observations have indicated much more ice than
99 known source could generate in clouds, especially with temperatures warmer than
100 about -15°C (e.g., Hobbs, 1969; Beard, 1992).

101 The U.S. DOE ARM Program (Stokes and Schwartz, 1994; Ackerman and
102 Stokes, 2003) conducted its M-PACE field campaign over the North Slope of Alaska
103 (NSA) during the period of 27 September - 22 October 2004 (Harrington and
104 Verlinde, 2004; Verlinde et al., 2007). During the field campaign, Arctic clouds were
105 measured in detail using a wide range of instruments such as the ARM millimeter
106 wavelength cloud radar (MMCR), micropulse lidar (MPL), laser ceilometers, and two
107 instrumented aircraft (Verlinde et al., 2007). ARM has also derived the CRM/SCM
108 (Single-Column Model) forcing data from a sounding network in the Arctic region for
109 a seventeen and a half day Intensive Operational Period in October 2004 (Xie et al.,
110 2006) by applying the constrained variational analysis approach developed by Zhang
111 and Lin (1997) and Zhang et al. (2001). The M-PACE observations (e.g., McFarquhar

112 et al., 2007) and the large-scale forcing data (e.g., Xie et al., 2006; Klein et al., 2006)
113 have been used to both initialize and evaluate the results of numerical simulations that
114 provide information on the physical processes that can explain the longevity of these
115 Arctic mixed-phase clouds and the distributions of hydrometeors within them.
116 Fridlind et al. (2007) studied ice formation using a large-eddy simulation (LES)
117 model. Luo et al. (2007b; Luo07 hereafter) tested the effects of microphysics
118 parameterizations with a CRM. Morrison et al. (2007a) examined the sensitivity to
119 cloud condensation and ice nuclei concentrations in a mesoscale model. An
120 intercomparison project between LES, CRM, and SCM models and observations have
121 focused on both the single-layer MPS clouds (Klein et al., 2007) and the more
122 complicated multiple-layer MPS clouds (Morrison et al., 2007b).

123 In this study, the University of California at Los Angeles/Chinese Academy of
124 Meteorological Sciences (UCLA/CAMS) CRM, which is the same as the CRM used
125 in Luo07, is used to simulate a three-and-a-half-day subperiod of M-PACE, during
126 which multiple-layer MPS clouds were observed at the NSA sites. In addition to the
127 contrast between single-layer MPS clouds and multiple-layer MPS clouds, there are
128 other differences in configurations of the simulations between Luo07 and this study.
129 Most importantly, the large-scale forcing data were constant during the 12 h
130 simulation period in Luo07 but vary with time during the three-and-a-half-day
131 simulation period here. Secondly, an ocean surface was assumed in Luo07 as the
132 clouds were caused by off-ice flow over the open ocean that was adjacent to the
133 northern coast of Alaska. A land surface is considered here. Accordingly, the surface
134 latent and sensible heat fluxes used in Luo07 were significantly larger (136.5 W m^{-2}
135 and 107.7 W m^{-2} , respectively) than those used in this study ($18 \pm 5 \text{ W m}^{-2}$ and $3 \pm 5 \text{ W}$
136 m^{-2}). The single-layer MPS clouds in Luo07 were maintained by the significant
137 surface turbulent fluxes. The formation and maintenance mechanisms for the

138 observed multiple-layer MPS are more complicated, which is the focus of the present
139 study.

140 Despite the rapid progress in the understanding of single-layer Arctic mixed-
141 phase clouds through modeling studies (e.g., Jiang et al., 2000; Morrison and Pinto,
142 2006; Fridlind et al., 2007), multi-layer Arctic mixed-phase clouds are seldom
143 modeled. The present modeling study attempts to increase the understanding of
144 physical mechanisms for the formation and maintenance of multi-layer Arctic clouds.
145 The objectives of this study are twofold. The first objective is to examine how well
146 the CRM simulates the occurrences and evolution of the multiple-layer MPS clouds
147 and their complex macroscopic and microphysical structures by comparing with the
148 M-PACE observations. The second goal is to explore the possible mechanisms for the
149 formation, maintenance, and decay of the multiple-layer MPS clouds. To achieve this
150 objective, a set of sensitivity experiments are performed to test the impacts of the
151 large-scale forcing, radiative cooling, surface heat flux, ice-phase microphysical
152 processes, and latent heating caused by phase change of hydrometeor.

153 Section 2 gives a description of the field measurements including the large-
154 scale environment, cloud properties and aerosol properties. The numerical
155 simulations are described in Section 3. Extensive analyses of the Baseline results are
156 presented in Section 4, including detailed simulation results and comparison with the
157 observations. Section 5 represents the results from the sensitivity experiments.

158 Section 6 contains the summary and conclusions.

159 **2. Field measurements**

160 **2.1 Large-scale environment**

161 The NSA was under three different synoptic regimes with two transition periods
162 during M-PACE (Verlinde et al. 2007). This study focuses on a three-and-a-half-day
163 subperiod (14Z 5 October to 02Z 9 October) of the second regime (between 4 and 13
164 October). This synoptic regime was featured by high pressure building over the pack ice

165 to the northeast of the Alaska coast. As the high pressure system dominated the NSA
166 until 15 October, a small midlevel low pressure system drifted along the northern Alaska
167 coast from 5 to 7 October, and dissipated between Deadhorse and Barrow on 7 October.
168 This midlevel low brought a considerable amount of mid- and upper-level moisture to the
169 NSA. The low-level northeasterly flow out of the high pressure and the small midlevel
170 disturbance related to the low pressure system combined to produce a complicated
171 multilayer cloud structure over the NSA.

172 **2.2 Cloud properties**

173 Clouds were observed by a wide range of instruments, which were deployed at the
174 ARM NSA surface sites (Barrow, Oliktok Point and Atqasuk; Figure 1) or aboard the two
175 aircraft participated in the M-PACE. The University of North Dakota (UND) Citation
176 served as an in situ platform. Cloud properties are derived from these surface and air-
177 based measurements. Liquid water path (LWP) and precipitable water vapor were derived
178 from the 2-channel (23.8 and 31.4 GHz) microwave radiometers (MWRs) deployed at the
179 ARM NSA surface sites (Turner et al., 2007). The time interval of the LWP is ~30 s.
180 Other cloud properties that are used in the present study are described here.

181 **2.2.1 Occurrences and locations of mixed-phase cloud layers**

182 Occurrences of the mixed-phase cloud layers, along with their base and top heights,
183 were determined by combining measurements from the MPL (Micropulse Lidar) and
184 MMCR (Millimeter Wavelength Cloud Radar) deployed at Barrow (Fig. 1). These
185 measurements were available at a time interval of ~35 s. The vertical resolution of the
186 MMCR is ~45 m and that of the MPL is ~30 m. Based on a technique discussed by Wang
187 and Sassen (2001), the cloud base height of the first water-dominated mixed-phase cloud
188 layer above the surface is derived from the MPL measurements. To provide the cloud top
189 height of the optically thick first cloud layer and the base and top heights of the upper
190 cloud layers, profiles of reflectivity (Z_e) and spectral width from the MMCR
191 measurements must be used, as MPL cannot penetrate a cloud layer with optical depth

192 larger than 3. The Z_e profiles provide information for the occurrence of hydrometeors,
193 especially the particles that are relatively large because Z_e is proportional to the sixth
194 power of particle diameter under Rayleigh scattering condition. Therefore, Z_e profiles
195 contain very limited information for the occurrences of water droplets in the mixed-phase
196 clouds as ice particles are at least several times larger than water droplets. To detect the
197 occurrences of water droplets in the mixed-phase clouds, the size distribution difference
198 between mixed-phase clouds (wider) and ice or water clouds (narrower), which can be
199 identified with the spectral width of MMCR, is used. When cloud transition from ice
200 precipitation to water dominated mixed-phase cloud, an increase in the spectral width is
201 normally observed. This characteristic is used to determine base and top heights of water
202 dominated mixed-phase clouds when MPL measurements are not useful. Compared to
203 single layer or first layer base and top heights, the upper layer base and top heights have
204 larger uncertainties (within 100 m versus 45 m).

205 **2.2.3 Bulk cloud microphysical properties**

206 The bulk microphysical properties of the multiple-layer MPS clouds were derived
207 from the UND Citation measurements on October 5, 6, and 8 (see details in Zhang et al.,
208 2007). The properties used in the present study include liquid water content (LWC), total
209 ice water content (IWC), total water droplet number concentration (n_c), and total ice
210 crystal number concentration (n_{is}). The bulk properties are available at a 10 s interval, but
211 represent a 30 s running average of the measured ice properties. A detailed description of
212 the procedure to derive the bulk microphysical properties of the MPS clouds and the
213 uncertainties associated with the derived products is found in McFarquhar and Cober
214 (2004) and McFarquhar et al. (2007). A concise description of the aircraft observations is
215 given below.

216 The UND Citation flew three missions dedicated to characterizing microphysics
217 of the multiple-layer MPS clouds on October 5, 6, and 8 by executing spiral ascents and
218 descents over Barrow and Oliktok Point and by flying ramped ascents and descents

219 between. A typical flight pattern that the UND Citation took was presented in Verlinde et
220 al. (2007; their Fig. 5). The mission on October 5 started from about 1930 UTC (1130
221 local time) and lasted about two hours and fifteen minutes. The second mission was
222 performed between 1830 UTC (1030 local time) and 2130 UTC (1330 local time)
223 October 6. The flight taken on October 8 lasted about two and half hours starting at about
224 2000 UTC (1200 local time). There are 628, 829, and 289 in-cloud observations obtained
225 during the three missions, respectively, covering a total in-cloud period of about five
226 hours. Here, *in-cloud* means the total condensed water content observed by the Citation
227 was greater than 0.001 g cm^{-3} . The numbers of the samples of LWC and IWC within
228 each of the 400 m height bin are represented in Figure 2. The sample numbers in the
229 height bins vary from zero to 210 with relatively more samples taken between 400 m and
230 2 km. There are no samples at heights below 400 m for all three missions and few
231 samples above 2 km for the October 5 and October 8 missions.

232 **2.3 Aerosol properties**

233 Aerosol size distribution and chemical composition are needed for the calculation
234 of droplet activation (Abdul-Razzak et al., 1998; Abdul-Razzak and Ghan, 2000) in the
235 CRM simulations. Ice nuclei (IN) concentration is needed for the purpose of calculating
236 heterogeneous ice nucleation in the CRM. In the absence of useful condensation nucleus
237 data for aerosol size distribution during the simulation period (14Z 5 October to 02Z 9
238 October), and because the IN concentrations from the Continuous Flow Diffusion
239 Chamber (CFDC; Rogers et al., 2001) aboard the Citation during this period show mean
240 values and scatter similar to those recorded on the October 9 and 10 flights, we specify
241 the aerosol properties and IN concentration based on the measurements obtained on
242 October 9 and 10, i.e. the same as in Luo07, Klein et al. (2007) and Morrison et al.
243 (2007b). It is further assumed that concentrations of aerosols and IN are horizontally and
244 vertically homogeneous in the CRM domain, except for the contact IN explained below.

245 A bimodal lognormal aerosol size distribution was fitted to the average size-
246 segregated Hand-Held Particle Counter (HHPC-6) measurement on October 10, with the
247 total aerosol concentration constrained by the average NOAA Earth System Research
248 Laboratory condensation nuclei measurements (Morrison et al., 2007a). The geometric
249 mean radii are 0.052 and 1.3 μm , standard deviations are 2.04 and 2.5, and the total
250 number concentrations are 72.2 and 1.8 cm^{-3} for the small and large modes of the aerosol
251 size distribution, respectively. The measurements of active IN concentration represent the
252 sum of IN with a diameter less than 2 μm acting in deposition, condensation-freezing,
253 and immersion-freezing modes. They indicate locally high concentrations of IN up to \sim
254 10 L^{-1} , and a mean of about 0.16 L^{-1} assuming that concentrations below the detection
255 threshold are zero. The observed mean IN number concentration is used in our CRM
256 simulations to represent the aforementioned nucleation modes. No direct measurements
257 are available for the number of IN acting in contact-freezing mode. Thus the contact IN
258 number is a function of temperature following Meyers et al. (1992).

259 3. Numerical simulations

260 The CRM used in this study is the UCLA/CAMS CRM, which was originally
261 developed by Steve Krueger and Akio Arakawa at UCLA (Krueger, 1988). A modified
262 version of this CRM (Xu and Krueger, 1991) was brought to the Colorado State
263 University (Xu and Randall, 1995) and later to NASA Langley Research Center (Xu et al.,
264 2005) where more modifications were made to the CRM (Cheng et al., 2004; Luo et al.
265 2007a, b). The CRM is based on the anelastic dynamic framework in 2 dimensions (x and
266 z) with a third-order turbulence closure (Krueger 1988). The two-moment microphysics
267 scheme of Morrison et al. (2005) and the radiative transfer scheme of Fu and Liou (1993)
268 are coupled to the dynamic core (Luo07). More details about the CRM, especially the
269 newly added prognostic variables of number concentrations of four hydrometeor types
270 (cloud water, cloud ice, rain and snow), are provided in Luo07.

271 Six numerical experiments are performed, including the Baseline simulation and
272 five sensitivity studies (Table 1). The Baseline simulation is prescribed with time-varying
273 large-scale advective tendencies of heat and moisture (Figs. 3a, b) and surface latent and
274 sensible fluxes (Fig. 3c). All simulations start from the same initial atmospheric state at
275 14 Z October 5 and are run for 84 hours. They are performed with the same grid spacing
276 of 2 km in the horizontal. The vertical grid spacing stretches from 100 m at the surface to
277 500 m at ~ 5 km and is 500 m above 5 km. The domain width is 256 km in the horizontal
278 and 20 km in the vertical. A time step of 5 seconds is used. Vertical velocity is specified
279 as zero at the upper and lower boundaries. Cyclic boundary conditions are used at the
280 lateral boundaries. At the lower boundary, the vertical turbulent fluxes of momentum are
281 diagnosed using flux-profile relationships based on Monin-Obukhov surface-layer
282 similarity theory (Businger et al., 1971). For radiation purpose, the spectral surface
283 albedos for the six bands of Fu and Liou (1993) radiative transfer scheme are determined
284 by combining the 3-hourly broadband albedo from the ARM analysis (Xie et al., 2006)
285 with a curve of spectral albedo over fresh snow. The curve of snow spectral albedo is
286 based on the data downloaded from the Clouds and the Earth's Radiant Energy
287 System/Surface and Atmospheric Radiation Budget (CERES/SARB) website
288 (ftp://snowdog.larc.nasa.gov/pub/surf/data_tables.asc). Figure 3d shows the spectral
289 albedos corresponding to a broadband albedo of 0.86. The skin temperature from the
290 ARM analysis is used in all simulations for the calculation of upward longwave (LW)
291 radiation. Radiative effects of the aerosols are not considered.

292 The sensitivity simulations (Table 1) consist of noLSadv, noSfcFlx, noLWrad, noIce,
293 and noMicLat simulations, which are identical to the Baseline simulation except that one
294 aspect of the experimental designs is artificially altered. These simulations are designed
295 as previous modeling studies suggest that large-scale advection, surface turbulent flux,
296 cloud top radiative cooling, and IFN (and hence ice crystals) may influence the formation
297 and evolution of Arctic clouds (e.g., Curry et al., 1997; Pinto, 1998; Harrington et al.,

298 1999; Harrington and Olsson, 2001) and effects of cooling (heating) caused by phase
299 change of hydrometeors on Arctic clouds are not clear. The noLSadv simulation neglects
300 the large-scale advective tendencies of temperature and water vapor mixing ratio
301 provided by the ARM analysis (Figs. 3a and 3b; Xie et al. 2006). The noSfcFlx
302 simulation assumes that the surface turbulent fluxes of sensible and latent heat are zero.
303 The noLWrad simulation sets the LW radiative cooling (heating) rates as zero¹. The
304 noIce simulation turns off all ice-phase microphysical processes. The noMicLat
305 simulation neglects the latent heating (cooling) due to microphysical processes.

306 **4. Baseline results**

307 **4.1 Temperature, moisture, surface precipitation**

308 The atmospheric temperature and water vapor mixing ratio (q_v) decrease with
309 height from nearly 0°C and $\sim 4 \text{ g kg}^{-1}$ at the surface to -24°C and 0.5 g kg^{-1} at $\sim 500 \text{ hPa}$
310 ($\sim 4.7 \text{ km}$) in the Baseline simulation (Figs. 4a and 4b). Typical differences in
311 temperature between the Baseline simulation and the ARM analysis (Xie et al., 2006;
312 Klein et al., 2006) are between -2°C and $+2^\circ\text{C}$ and those in q_v are between -0.25 g kg^{-1}
313 and 0.25 g kg^{-1} . The largest differences are located around 800 hPa, where the Baseline
314 simulation is too cold and dry (up to -4 K and -0.5 g kg^{-1} , respectively) before 48 h and
315 too warm and moist (up to 4 K and 0.5 g kg^{-1} , respectively) after 48 h (Figs. 4c, 4d). The
316 interactions between clouds and radiation in the simulation may be the reason for these
317 large differences. As will be shown later, ice crystals are underestimated and cloud water
318 content is probably overestimated at 12-24 h in the simulation, resulting in extra radiative
319 cooling and negative temperature biases near the cloud top before 48 h due to the
320 different optical properties of ice crystals and water droplets. The negative q_v biases
321 before 48 h may be caused by excessive conversion from vapor to liquid due to excessive

¹ We also performed another simulation in which the effects of both longwave and shortwave radiation are ignored. The results from this simulation are essentially the same as those from the noLWrad simulation and, therefore, are not included in this paper.

322 radiative cooling, which enhances the cloud-scale circulation. The overestimation in
323 temperature after 60 h may be partially due to the strong large-scale advective heating at
324 51-54 h period ($\sim 9 \text{ K day}^{-1}$; Figure 3a). The overestimation in both temperature and
325 moisture after 60 h may also due to the inadequate simulation of clouds around 48 h, as
326 suggested by time series of both surface precipitation and liquid water path shown later.

327 Figure 4e shows the 3-hourly time series of surface precipitation rate (mm day^{-1})
328 from the ARM analysis (Xie et al., 2006) and the Baseline simulation. The ARM analysis
329 indicates five precipitation events with peaks at 6 h, 24 h, 33 h, 44 h, and 70 h,
330 respectively. Due to the blowing snow conditions and inadequate surface measurements,
331 the magnitude of surface precipitation during M-PACE can be biased (Xie et al. 2006).
332 The Baseline simulation captures the timing of three observed precipitation peaks, with
333 magnitudes that are smaller than or comparable to the observations. The first peak at 8 h
334 was not captured and delayed to 14 h, due to the model spinup. The peak at 44 h was not
335 simulated at all.

336 ~~336~~ 4.2 Cloud properties

337 To examine the temporal evolution of the cloud vertical structure, the time-height
338 cross section of the horizontally averaged liquid water content (LWC) and ice plus snow
339 water content (ISWC) from the Baseline simulation is shown in Figure 5a. Major features
340 of the simulated cloud structures are as follows. First, there are two overlapping mixed-
341 phase cloud layers separated by ice precipitation shafts during most of the simulation
342 period. Second, within the mixed-phase cloud layers, the amount of LWC is about one or
343 two orders of magnitude larger than that of ISWC. Third, the amount of LWC and the
344 locations of the mixed-phase cloud layers, especially the top height of the upper cloud
345 layer, vary with time. The statistics of the simulated cloud properties are compared with
346 the ARM observations below.

347 4.2.1 Occurrences of multiple-layer MPS clouds

348 One of the unique features of the Arctic MPS clouds under study is that there are
349 multiple mixed-phase cloud layers coexisting. Statistics of their occurrences are
350 computed using the MMCR-MPL observations at Barrow. To compare with the
351 observations, the number of mixed-phase cloud layers at each individual CRM grid
352 column, as well as the base and top heights of the cloud layers, is determined by
353 analyzing the profiles of cloud water mixing ratio (q_c) and cloud ice plus snow mixing
354 ratio (q_{is}) at a 5-min temporal interval from the Baseline simulation. A grid cell is
355 considered as cloudy if q_c is larger than 0.01 g kg^{-1} and q_{is} is larger than 0.0001 g kg^{-1} ;
356 otherwise, it is clear. Using a threshold value of 0.0001 g kg^{-1} for both q_c and q_{is} causes
357 an increase in the occurrence frequency of 1% and 2%, respectively, for three-layer and
358 double-layer mixed-phase clouds and a decrease of 1% for single-layer mixed-phase
359 clouds. However, the major analysis results remain unchanged.

360 The occurrences and relative occurrence frequencies of single-, double-, and three-
361 layer mixed-phase clouds from the observations and the Baseline simulation are shown in
362 Table 2. During 6 and 7 October, the observations reveal the occurrences of mostly
363 single- or double-layer clouds with a small amount of three-layer clouds (9% on October
364 6 and 3% on October 7). The fractions of the observed single-layer clouds are 49% on
365 October 6 and 66% on October 7 and those of the double-layer clouds are 41% and 31%.
366 The Baseline simulation produces a small amount of three-layer cloudy columns (7% and
367 1%, respectively), which are comparable to the observational results. The fractions of the
368 single-layer cloudy columns are 29% and 63%, respectively, for October 6 and October 7,
369 and those of the double-layer cloudy columns are 63% and 36%. The increase of the
370 single-layer cloud fraction and decrease of the double-layer cloud fraction, respectively,
371 from October 6 to October 7, are consistent with the observations.

372 For October 8, 90% of the observed clouds is single-layer and 10% is double-layer.
373 The Baseline simulation produces a larger fraction for the single-layer clouds (66%) than
374 for the double-layer clouds (34%), qualitatively consistent with the observations. These

375 results suggest that the Baseline simulation reasonably reproduced the occurrences of the
376 multiple-layer MPS clouds as revealed by the statistics of MMCR-MPL observations.

377 **4.2.2 Mixed-phase cloud layer boundaries**

378 An adequate simulation of cloud base and top heights is important since they are
379 highly correlated with the downward LW radiative flux at the surface and the outgoing
380 longwave radiation (OLR) at the top-of-the-atmosphere (TOA), respectively. The top and
381 base heights of the first and second MPS cloud layers are, hereafter, compared between
382 the Baseline simulation (12-84 hr) and the MMCR-MPL observations (October 6-8)
383 because clouds with more than two layers are rare, as shown in Table 2.

384 Figure 6 shows the histograms of cloud base height, cloud top height, and physical
385 thickness of the first mixed-phase cloud layer above the surface from the Baseline
386 simulation (left panels) and the MMCR-MPL observations (right panels). Distribution of
387 the observed cloud base height shows a mode at 625 m with about 70% between 250 m
388 and 1 km (Fig. 6d). Distribution of the observed cloud top height has a mode at 1.125 km
389 and about 70% between 750 m and 1.5 km (Fig. 6e). Compared to the observations, the
390 Baseline cloud bases and tops are lower. The cloud-base-height distribution has a mode at
391 the lowest bin (0-250 m) and about 70% below 500 m (Fig. 6a). The cloud-top-height
392 distribution shows a mode of 875 m and ~ 60% below 1 km (Fig. 6b). Too many
393 occurrences of the clouds near the surface are probably related to the moist bias below
394 900 hPa (~ 800 m) in the simulation (Fig. 4d). Both the observations and the Baseline
395 suggest that most of the cloud layers are physically thin (Figs. 6f and 6c) with about 93%
396 and 80%, respectively, of the clouds being thinner than 750 m.

397 The observed cloud bases (tops) of the second cloud layers are distributed quite
398 evenly between 1 km and 4 km (Figs. 7d and 7e). These cloud layers are physically thin
399 with thicknesses less than 500 m (Fig. 7f). The histograms from the Baseline simulation
400 appear significantly different from the observed ones. The simulated cloud-base-height
401 has a bimodal distribution. The mode at ~ 3.2 km is mainly caused by the clouds near the

402 end of the simulation period (Fig. 5a). The other mode at ~1.5-2.0 km is associated with
403 the clouds during 12-36 h simulation period. The simulated tops are located at a few bins
404 (Fig. 7b), which can also be seen from Fig. 5a. The simulated clouds are physically
405 thicker than the observed (Figs. 7c and 7f).

406 Several factors may be responsible for the discrepancies in the vertical locations of
407 the MPS cloud layers between the Baseline and MMCR-MPL observations. The large-
408 scale forcing data used to drive the CRM may contain errors (Xie et al., 2006), possibly
409 caused by the low data density during M-PACE and/or associated with the background
410 field used to generate the forcing data, which was generated by the ECMWF (European
411 Centre for Medium range Weather Forecasting) model. The vertical resolutions of the
412 forcing data and the CRM grid are a few hundred meters, coarser than that of the MMCR
413 (30 m) and MPL (45 m). Uncertainties associated with the model's physics, such as
414 turbulence and microphysics, cannot be ruled out as possible causes of the discrepancies.

415 **4.2.3 Liquid water path (LWP)**

416 The vertically integrated liquid water amount, i.e. liquid water path (LWP), is
417 compared between the Baseline and the MWR-based retrievals (Turner et al., 2007) for
418 the ARM surface sites at the NSA (Barrow, Atqasuk, and Oliktok Point). When
419 temporally averaged over 78 hr starting from 20 Z October 6, i.e. the first 6 h of the
420 simulation period is excluded in the averaging, the Baseline domain-averaged LWP is
421 about the same as the MWR-based LWP averaged at the three sites (79 g m^{-2} versus 81 g
422 m^{-2}). However, the time series of the simulated and retrieved LWPs exhibit different
423 variations with time (Fig. 8). The simulated LWP decreases with time from 12 h to 48 h
424 and increases at ~ 60 h. The retrieved LWP is relatively more constant with time.

425 The discrepancy between the simulated and retrieved LWPs could be related to
426 possible errors associated with the simulation (e.g. forcing data, microphysics). On the
427 other hand, the retrievals are available at only three sites and there was significant
428 horizontal inhomogeneity in LWP over the simulation area. Therefore, the retrievals

429 averaged among the three sites may not represent the evolution of the domain-averaged
430 LWP very well. The inhomogeneity is indicated by the significant differences in the
431 retrieved LWPs among the three sites. The temporally averaged values are 124 g m^{-2}
432 (Barrow), 61 g m^{-2} (Oliktok Point), and 57 g m^{-2} (Atqasuk), respectively. The retrieved
433 LWPs temporally evolve with distinct patterns among the three sites (not shown).

434 **4.2.4 Bulk microphysical properties**

435 The bulk microphysical properties of the MPS clouds including LWC, n_c , total ice
436 water content (i.e. ISWC), and total ice crystal number concentration (n_{is}), which are
437 derived from the Citation measurements obtained during the missions taken on October 5,
438 6 and 8 (Zhang et al., 2007), are compared to those from the Baseline simulation during
439 the subperiods of 12-24 h, 24-36 h, and 72-84 h, respectively. The three subperiods are
440 denoted as subperiods A, B, and C hereafter. Note that the number of the observed
441 samples is limited (Fig. 2). The Student's t-test is performed for the simulated and
442 observed LWC, n_c , ISWC, and n_{is} , respectively. Due to the vertical variation of the
443 Citation sample numbers (Fig. 2), the simulated LWC and n_c located between 400 m and
444 2 km during the subperiods A and C and those located between 400 m and 4 km during
445 the subperiod B are used in the Student's t-test, whereas the simulated ISWC and n_{is}
446 located between 400 m and 4 km during the subperiods A, B, and C are used. Results
447 from the Student's t-test (Table 3) suggest that the simulated and observed cloud
448 properties have significantly different means, except for the LWC during the subperiod B.
449 The Student's T-statistics suggest that the simulated means of LWC and n_c are relatively
450 closer to the observed means than those of ISWC and n_{is} .

451 Although the simulated and observed means are significantly different, the
452 Baseline simulation qualitatively reproduced the major characteristics in the vertical
453 distributions and temporal variations of LWC, n_c , ISWC and n_{is} suggested by the Citation
454 measurements (Figs. 9-12), as to be discussed below. Because the model will never

455 perfectly simulate the environment where the clouds form, it is the qualitative
456 comparison that is more useful.

457 **a. Cloud liquid water content**

458 The observations indicate that there are large temporal variations in vertical
459 distribution of the LWC. For example, at heights of ~ 1 km, the means and variations of
460 LWC are larger on October 8 than those on October 5 and 6 (Figs. 9d-f). This change is
461 qualitatively reproduced by the Baseline (Figs. 9a-c). The LWCs obtained during the
462 October 5 mission have average values of about 0.05 g m^{-3} at heights between 400 m and
463 1.6 km, with standard deviations that are with about the same magnitudes as the averages
464 (Fig. 9d). At the same heights, the Baseline LWCs averaged over the subperiod A are
465 $0.06\text{-}0.08 \text{ g m}^{-3}$ (Fig. 9a). For the subperiod B, both the observations and the Baseline
466 suggest that the LWCs have a relatively constant vertical distribution at 500 m - 3.5 km
467 with averages of about $0.05\text{-}0.1 \text{ g m}^{-3}$ (Figs. 9b and 9e). During the subperiod C, the
468 observed LWCs increase with height from 0.06 g m^{-3} at 600 m to 0.15 g m^{-3} at ~ 1.0 km,
469 with variations which are comparable to or larger than the means. The simulated LWCs
470 increase with height from about 0.06 g m^{-3} at 500 m to 0.20 g m^{-3} at ~ 1 km, generally
471 consistent with the observations.

472 Both the aircraft observations (McFarquhar et al., 2007) and the CRM results
473 (Luo07) suggested that, LWC increases with height within the single-layer mixed-phase
474 clouds occurred during a subperiod of the M-PACE, as a result of adiabatic growth of
475 liquid water droplets when ascend in the updraft. The trend of LWC with altitude here
476 looks different because of the large variations in cloud base height in both the
477 observations (Figs. 6d and 7d) and the simulation (Figs. 6a and 7a).

478 **b. Cloud droplet number concentration**

479 The observations reveal that the droplet number concentrations are generally low
480 during the three missions, with means of about $10\text{-}30 \text{ cm}^{-3}$ and variations of about the
481 same magnitude as the means. The Baseline n_c is less than 60 cm^{-3} . Vertical distributions

482 of the Baseline n_c are similar between the subperiods A and B. The simulated n_c during
483 the two subperiods decreases with height within the lower cloud layer and is relatively
484 constant within the upper cloud layer. There is no observation below 400 m to evaluate
485 the simulated results, however. During the subperiod C, the simulated n_c in the lower
486 cloud layer is about two times of that from the observations ($30\text{-}40\text{ cm}^{-3}$ versus $\sim 15\text{ cm}^{-3}$).
487 In the upper cloud layer, the simulated n_c has a value of $20\text{-}40\text{ cm}^{-3}$, comparable to the
488 observations ($20\text{-}30\text{ cm}^{-3}$).

489 The decrease of n_c with height in the first cloud layer above the surface (Figs. 10a
490 and 10b) differs from the constant vertical distribution of n_c in the single-layer MPS
491 clouds (McFarquhar et al., 2007; Luo07). In the simulation, the magnitude of n_c is mainly
492 determined by the activation of cloud condensation nuclei (CCN). The CCN activation is
493 calculated following the parameterization of Abdul-Razzak et al. (1998) and Abdule-
494 Razzak and Ghan (2000), which relates the aerosol size distribution and composition to
495 the number activated as a function of maximum supersaturation using the Köhler theory.
496 The maximum supersaturation is related to not only the thermodynamic characteristics of
497 atmosphere and aerosol properties but also the effective vertical velocity, which in turn is
498 related to the resolved-scale and parameterized subgrid-scale vertical velocities and
499 radiative cooling. For the first cloud layer above the surface, the production of n_c is
500 dominated by the subgrid-scale vertical velocity, which decreases with height below 1
501 km (not shown).

502 **c. Total ice water content and ice crystal number concentration**

503 Observations from the October 5 and October 6 missions suggest that the total
504 IWCs have larger mean values and standard deviations at heights of 400 m - 1.5 km
505 ($0.05\text{-}0.1\text{ g m}^{-3}$) than those at higher levels ($<0.05\text{ g m}^{-3}$) (Figs. 11d and 11e). This
506 vertical variation in IWC is reproduced by the Baseline simulation (Figs. 11a and 11b).
507 The major discrepancy in IWC between the observations and the Baseline is that the

508 simulated ISWC is a few times smaller compared to the observed total IWC at the same
509 height range except for near the surface where no observations are available.

510 Both the observations (Figs. 12d-f) and the Baseline results (Figs. 12a-c) suggest
511 more ice crystals in the lower MPS cloud layer than in the upper cloud layer. In the
512 Baseline simulation, this is mainly caused by the H-M mechanism (Hallet and Mossop,
513 1974), which is the only mechanism for ice enhancement included in the CRM's
514 microphysics scheme and operates at temperatures between -8°C and -3°C . The ice
515 crystal number concentration is increased by the H-M mechanism at a horizontal-average
516 rate of several $\text{L}^{-1} \text{hr}^{-1}$. However, the simulated number concentrations of ice crystals are
517 about one order of magnitude smaller than the observed ones, suggesting that some ice
518 production mechanisms might be missing in the cloud microphysics scheme.

519 The underestimate of n_{is} by the simulation was previously seen in the simulation of
520 the single-layer MPS clouds (e.g., Luo07; Fridlind et al., 2007), where ice enhancement
521 through the H-M mechanism was not significant because the temperature ranged from -
522 15°C (cloud top) to -10°C (cloud base), colder than the temperatures at which the H-M
523 mechanism operates.

524 **5 Results from sensitivity experiments**

525 **5.1 Time-height distribution of clouds**

526 The time-height cross sections of the horizontal-averaged LWC and ice plus snow
527 water content (ISWC) from the sensitivity experiments (Fig. 13) are compared to those
528 from the Baseline simulation (Fig. 5a) in order to examine the possible effects of surface
529 latent and sensible heat fluxes, large-scale advective forcing, LW radiative cooling, ice
530 crystals, and heating caused by phase change on the simulated cloud vertical structure
531 and temporal evolution.

532 The lower MPS cloud layer above the surface is significantly weakened and
533 disappears after 36 h in the noSfcFlx experiment (Fig. 13a). This suggests that the lower
534 MPS cloud layer in the Baseline simulation is closely related to the surface fluxes. The

535 atmosphere at heights below ~ 1 km is drier in noSfcFlx than in Baseline (Fig. 14b). The
536 differences in q_v between Baseline and noSfcFlx accumulate with time and are about 1 g
537 kg^{-1} near the surface during the last 36 h. The differences in potential temperature (Θ)
538 are more complicated both temporally and vertically. Before 48 h, the surface heat fluxes
539 cause an increase in Θ at heights below ~ 1 km. After 48 h, the Baseline produces
540 warmer (colder) atmosphere at heights below ~ 500 m (500 m – 2.5 km). The large
541 negative values at 500 m -1 km after 48 h are related to the large radiative cooling rates
542 near the cloud top in the Baseline simulation (about -15 K day^{-1} ; Fig. 5b).

543 The noLSadv produces single-layer MPS clouds with tops rising with time from
544 below 1 km at 6-12 h to ~ 3 km near the end of the simulation (Fig. 13b). Compared to
545 the LWC of the first mixed-phase cloud layer in the Baseline, the noLSadv LWC is about
546 one order of magnitude larger, caused by significantly stronger LW radiative cooling near
547 the cloud top (about -20 K day^{-1} ; not shown) and enhanced cloud-scale dynamical
548 circulation (shown later). The upper MPS cloud layer formed in the Baseline (Fig. 5a)
549 does not appear in the noLSadv experiment. This suggests that the cooling and
550 moistening effects due to large-scale advection at the beginning of the simulation period
551 (Figs. 3a and 3b) may trigger the formation of the upper MPS cloud layer.

552 The noLWrad experiment produces two events of single-layer MPS clouds at 6-48
553 h and 62-84 h, respectively (Fig. 13c). The clouds of the first event have tops that are a
554 few hundred meters higher than their counterparts in Baseline. The second event occurs
555 later with smaller amount of LWC than in Baseline. The upper MPS cloud layer in
556 Baseline does not occur in noLWrad. In the Baseline (Fig. 5b), significant LW radiative
557 cooling/heating is associated with the single-layer clouds and the upper cloud layer when
558 multi-layer clouds coexist at a time, where the 3-hourly and horizontal-averaged LW
559 radiative cooling rates reach $\sim 20 \text{ K day}^{-1}$ near the cloud top and cloud base warms by a
560 few K day^{-1} . The LW radiative cooling is negligible in the first cloud layer located below
561 other clouds during 12-48 h. Combined with the results of the noLSadv experiment (Fig.

562 13b), these noLWrad results suggest that (a) the upper MPS cloud layer in the Baseline is
563 probably initialized by the large-scale advective forcing and maintained through the LW
564 radiative cooling near the cloud top, and (b) the LW radiative cooling could contribute to
565 more LWC, probably through enhancement of the cloud-scale dynamical circulation.

566 The noIce experiment produces cloud distributions (Fig. 13d) that are significantly
567 distinct from those in Baseline (Fig. 5a). Most importantly, a larger magnitude of LWC is
568 generated by the noIce experiment. The temporally averaged LWP (224 g m^{-2}) is
569 increased by a factor of 3 compared to the Baseline (79 g m^{-2}), suggesting the depletion
570 of liquid droplets by ice crystals in the Baseline. The larger noIce LWP probably results
571 from the interactions between the simulated clouds and radiation, as more liquid droplets
572 could result in a stronger radiative cooling which favors more condensation and thus a
573 positive feedback could be formed.

574 The noMicLat experiment produces cloud distributions (Fig. 13d) that are generally
575 similar to those in Baseline (Fig. 5a). One distinct feature, however, is that the noMicLat
576 experiment produces a larger amount of LWC in the interior of the MPS cloud layers.
577 Phase change of the hydrometeors causes a warming effect of several K day^{-1} near the
578 cloud top in the Baseline simulation (Fig. 5c), which partially cancels out the strong LW
579 radiative cooling effect there (Fig. 5b). Artificial ignorance of this warming effect due to
580 microphysical processes could result in a stronger net cooling effect near the cloud top,
581 which favors more condensation than in the Baseline simulation.

582 **5.2 Resolved- and subgrid-scale kinetic energy**

583 To explore possible effects of the processes on dynamical circulations, the resolved
584 kinetic energy (RKE) and turbulent kinetic energy (TKE) are analyzed for the CRM
585 simulations to examine the strength of the resolved and parameterized subgrid-scale
586 dynamical circulations, respectively. The RKE at each grid point is defined as
587 $(u'u'+v'v'+w'w')/2$, where u' , v' , and w' are the deviations of the velocities in the x-, y-,
588 and z-directions from their horizontal averages. Vertical profiles of the horizontally and

589 12-84 h averaged RKE, as well as the variation measured by standard deviation, are
590 compared among the simulations (Fig. 15).

591 First, the vertical variations of RKE in the simulations are closely related to the
592 simulated cloud fields (Fig. 5a and Figs. 13a-e). The RKE in the Baseline simulation has
593 smaller mean values ($\sim 0.1 \text{ m}^2 \text{ s}^{-2}$) at heights of $\sim 1.5 \text{ km}$ and larger mean values (~ 0.25
594 $\text{ m}^2 \text{ s}^{-2}$) at the heights where the MPS cloud layers occur, with variations that are
595 comparable to the means in magnitude (Fig. 15a). Compared to the Baseline, the resolved
596 circulation is significantly weakened at the heights below 1.5 km in the noSfcFlx
597 experiment (Fig. 15b), supporting the suggestion that the surface turbulent fluxes
598 contribute to the development of the low cloud layer in Baseline. Second, the RKE in the
599 noLSadv experiment has large mean values of $\sim 0.7 \text{ m}^2 \text{ s}^{-2}$ at heights between 400 m and
600 1.5 km (Fig. 15c), where a large amount of LWC is produced (Fig. 13b). The strong
601 radiative cooling near the cloud top is the major driver for the resolved-scale circulation
602 in this simulation. Third, the noLWrad experiment RKE is significantly smaller than that
603 in the Baseline at heights above 1.5 km . This suggests that there are significant impacts
604 of LW radiative cooling on the formation/maintenance of the upper-layer clouds and their
605 resolved-scale dynamical circulations. The noIce RKE at heights above 3 km is larger
606 than that in the Baseline, due to the artificially formed liquid-phase cloud layer in the
607 noIce experiment (Fig. 13d), which enhances the resolved dynamical circulation probably
608 through the stronger LW radiative cooling near the liquid cloud layer top. Lastly, the
609 noMicLat experiment produced RKE (Fig. 15f) is relatively constant with height (0.1 m^2
610 s^{-2}) and smaller than that in the Baseline by a factor of ~ 2 . Thus, the impact of latent heat
611 on resolved-scale circulations is not negligible throughout the cloud layer.

612 The mean values and variations of TKE in the simulations are generally smaller
613 than those of RKE except for near the surface where the mean TKE is larger ($\sim 0.8\text{-}1.0 \text{ m}^2$
614 s^{-2}). The mean TKE decreases with height to nearly zero at 1.5 km , suggesting that the
615 subgrid-scale vertical velocity decreases with height and causes a decrease in n_c with

616 height (Figs. 10a and 10b). The TKE is essentially zero at heights where clouds rarely
617 occur in the simulations. There is, however, one interesting result worth pointing out.
618 Compared to the Baseline, the noSfcFlx experiment produces a slightly larger TKE near
619 the surface ($1.0 \text{ m}^2 \text{ s}^{-2}$ versus $0.8 \text{ m}^2 \text{ s}^{-2}$) where few MPS clouds are produced in noSfcFlx.
620 This, combined with smaller RKE near the surface in the noSfcFlx than in the Baseline,
621 indicates that the lower MPS cloud layer in Baseline are more likely to be related to the
622 resolved circulation than to the parameterized subgrid-scale circulation. The source of
623 moisture, however, appears to be the surface turbulent flux of latent heat.

624

625 **6 Summary and conclusions**

626 Multiple-layer mixed-phase stratiform (MPS) clouds that occurred during a three-
627 and-a-half-day subperiod of the DOE-ARM Program M-PACE have been simulated
628 using a CRM. This CRM includes an advanced two-moment microphysics scheme
629 (Morrison et al., 2005), a state-of-the-art radiative transfer parameterization (Fu and Liou,
630 1993), and a complicated third-order turbulence closure (Krueger, 1988). Concurrent
631 meteorological, aerosol, and ice nucleus measurements are used to initialize the CRM.
632 Time-varying large-scale advective tendencies of temperature and moisture and surface
633 sensible and latent heat fluxes (Xie et al., 2006; Klein et al., 2006) are prescribed to the
634 CRM simulations. The Baseline simulation results have been extensively analyzed and
635 compared to the M-PACE observations, including the analysis of atmospheric
636 temperature and moisture biases, surface precipitation rate, and a variety of cloud
637 properties. Several sensitivity simulations have been performed, in addition to the
638 Baseline simulation, to provide insight into the processes modulating the formation and
639 evolution of the cloud layers.

640 The ARM analysis (Xie et al., 2006) suggests the occurrences of several
641 precipitation events during the simulation period. The CRM captures the timing of the
642 three of the five events except for the first event due to model spin up and the fourth
643 event due to underestimate of clouds. The magnitudes of the simulated precipitation are
644 smaller or comparable to the ARM observations. The magnitude of the simulated liquid
645 water path agrees with the observed, but its temporal variations are more pronounced
646 than the observed (Turner et al. 2007). The MMCR-MPL measurements reveal mostly
647 single- or double-layer MPS clouds at Barrow. The Baseline simulation reasonably
648 reproduces the relative frequencies of occurrence of the single- and double-layer MPS
649 clouds. However, there are several discrepancies in the vertical locations of the MPS
650 clouds between the Baseline simulation and the MMCR-MPL observations. Especially,
651 the bases and tops of the simulated lower MPS cloud layer are too low and the physical
652 thicknesses of the simulated upper MPS cloud layer appear too large.

653 The bulk microphysical properties derived from the Citation aircraft measurements
654 taken on October 5, 6, and 8 (Zhang et al., 2007) have been compared to the Baseline
655 results. The observations reveal that the LWCs taken during the October 5 and October 6
656 missions have relatively constant vertical distributions with means of about $0.05\text{-}0.1\text{ g m}^{-3}$
657 whereas those of October 8 have maxima at heights of $\sim 1\text{ km}$ ($\sim 0.15\text{ g m}^{-3}$) and $\sim 2.5\text{-}$
658 3.0 km ($\sim 0.01\text{ g m}^{-3}$). The droplet number concentrations (n_c) have mean values of $10\text{-}40$
659 cm^{-3} . The ISWC and n_{is} are several times larger in the lower MPS cloud layer ($\sim 0.05\text{ g m}^{-3}$
660 and a few tens L^{-1}) than in the upper MPS cloud layer. Comparison of the simulation
661 with these measurements indicates that the Baseline simulation can qualitatively
662 reproduce the major characteristics in the vertical structures and temporal variations of

663 LWC, n_c , ISWC, and n_{is} . However, the means of the cloud properties differ significantly
664 between the Baseline and the observations. Especially, the simulated n_{is} is one order of
665 magnitude smaller than the observed. This is consistent with the simulation of single-
666 layer MPS clouds performed by Luo et al. (2007), which suggested that some ice
667 formation processes might be missing in the two-moment microphysics scheme.

668 Possible causes for the discrepancies in the cloud properties between the Baseline
669 simulation and the M-PACE observations include errors associated with both the large-
670 scale forcing and the model physics. Especially, the underestimation of n_{is} by models
671 (LES, CRM, SCM) has been noticed by other modeling studies (e.g., Fridlind et al., 2007;
672 Luo07; Morrison et al, 2007b). This lends support to the hypothesis that some ice
673 forming mechanisms may be missing in the microphysics schemes. On the other hand,
674 the discrepancies could also be related to the small number of samples in the M-PACE
675 observations and uncertainties associated with the algorithms used to derive the cloud
676 properties.

677 Analyses of the sensitivity experiments indicate that the surface latent and sensible
678 heat fluxes, large-scale advective tendencies of temperature and moisture, LW radiative
679 cooling, existence of ice crystals, and heating due to phase change of hydrometeors play a
680 different role in modulating the evolution of the MPS cloud layers. The surface latent and
681 sensible heat fluxes used in the present study are small ($18 \pm 5 \text{ W m}^{-2}$ and $3 \pm 5 \text{ W m}^{-2}$,
682 respectively) compared to those in Luo07 (136.5 W m^{-2} and 107.7 W m^{-2} , respectively)
683 and Harrington and Olsson (2001; about 150 and 300 W m^{-2} , respectively). However, the
684 lower MPS cloud layer could not be formed when the surface latent and sensible heat
685 fluxes are ignored in one sensitivity experiment, suggesting the importance of the surface

686 fluxes to the lower MPS cloud layer. The upper MPS cloud layer could not be formed or
687 maintained if either the large-scale advective forcing or the LW radiative cooling is
688 artificially turned off in the simulation. These results suggest that the upper MPS cloud
689 layer is probably initialized by the large-scale advective forcing and maintained by the
690 strong LW radiative cooling near the cloud top through the interactions between the LW
691 radiative cooling and clouds, which results in stronger resolved-scale dynamical
692 circulations. When the ice-phase microphysical processes are artificially turned off, the
693 LWP is increased by a factor of three and the cloud vertical distribution and temporal
694 evolution differ significantly from the Baseline and the observations. Neglecting the
695 heating (cooling) caused by phase change of hydrometeors results in MPS clouds that
696 have larger LWCs and higher tops than in the Baseline because the net cooling is stronger
697 in the cloud layer. Moreover, the kinetic energy explicitly resolved by the CRM appears
698 to have contributed more greatly to the MPS clouds than the subgrid-scale TKE despite
699 of larger values of TKE near the surface layer.

700 The major contribution of this study is twofold. First, it provides a detailed,
701 statistical comparison between the observed and CRM-simulated multi-layer MPS cloud
702 properties, especially the macroscopic properties of the lower-and upper-cloud layers and
703 the vertical structures and temporal variations of the cloud microphysical properties. Such
704 a comparison provides a framework for future modeling studies of multi-layer clouds of
705 any type. Second, the sensitivity experiments provide some basic understanding of
706 physical mechanisms for formation and maintenance of multi-layer Arctic clouds. These
707 sensitivity simulations will also be useful to interpret the results of model
708 intercomparison of this M-PACE subperiod (Morrison et al., 2007b) because of different

709 physical parameterizations used in the models participated in the intercomparison. Future
710 studies of other similar cases will be helpful to confirm the conclusions drawn from this
711 study.

712

713 **Acknowledgments**

714 Research of Y. Luo was supported partially by research project from the Chinese
715 Academy of Meteorological Sciences and partially by the U.S. NASA CMAI. Work of
716 K.-M. Xu was supported by the U.S. NASA CMAI as part of the Modeling, Analysis and
717 Prediction (MAP) Program. H. Morrison is grateful for support through the National
718 Center for Atmospheric Research Advanced Study Program, Atmospheric Radiation
719 Measurement (ARM) Program of the U.S Department of Energy (DOE) (DE-FG02-
720 03ER63539), and NASA MAP (NNG06GBB1G). Research of G. McFarquhar and G.
721 Zhang was supported by the DOE-ARM (DE-FG02-02ER63337). Support of Z. Wang
722 was from the DOE-ARM (DE-FG02-05ER64069). Data were obtained from the ARM
723 program archive, sponsored by the Office of Biological and Environmental Research of
724 the U.S. Department of Energy. The authors thank Drs. Anthony Prenni and Paul DeMott
725 of the Colorado State University for providing the IN measurements and Dr. David
726 Turner of the University of Wisconsin-Madison for providing the LWP retrievals.

727

727

References

728

729 Abdul-Razzak, H., and S. J. Ghan, 2000: A parameterization of aerosol activation. 2.

730 Multiple aerosol types. *J. Geophys. Res.*, **105**, 6837-6844.

731 Abdul-Razzak, H., S. J. Ghan, and C. Rivera-Carpio, 1998: A parameterization of aerosol

732 activation. 1. Single aerosol types. *J. Geophys. Res.*, **103**, 6123-6131.

733 Ackerman, T., and G. Stokes, 2003: The Atmospheric Radiation Measurement Program.

734 *Phys. Today*, **56**, 38-45.

735 ACIA, 2005: *Impacts of a Warming Arctic: Arctic Climate Impact Assessment*.

736 Cambridge University Press, 144 pp.

737 Beard, K. V., 1992: Ice initiation in warm-base convective clouds: An assessment of

738 microphysical mechanisms. *Atmos Res.*, **28**, 125-152.

739 Businger, J. A., J. C. Wyngaard, Y. Izumi, and E. F. Bradley, 1971: Flux-profile

740 relationships in the atmospheric surface layer. *J. Atmos. Sci.*, **28**, 181-189.

741 Cheng, A., K.-M. Xu, and J.-C. Golaz, 2004: The liquid-water oscillation in modeling

742 boundary-layer cumuli with third-order turbulence closure models. *J. Atmos. Sci.*,

743 **61**, 1621-1629.

744 Curry, J. A., W. B. Rossow, and J. L. Schramm, 1996: Overview of Arctic cloud and

745 radiation properties. *J. Climate*, **9**, 1731-1764.

746 Curry, J. A., J. O. Pinto, T. Benner, and M. Tschudi, 1997: Evolution of the cloudy

747 boundary layer during the autumnal freezing of the Beaufort Sea. *J. Geophys. Res.*,

748 **102**, 13,851-13,860.

- 749 Curry, J. A., and Coauthors, 2000: FIRE Arctic Clouds Experiment. *Bull. Amer. Meteor.*
750 *Soc.*, **81**, 5-29.
- 751 Fridlind, A. M., A. S. Ackerman, G. McFarquhar, G. Zhang, M. R. Poellot, P. J. DeMott,
752 A. J. Prenni, and A. J. Heymsfield, 2007: Ice properties of single-layer
753 stratocumulus during the Mixed-Phase Arctic Cloud Experiment (M-PACE): Part
754 II, Model results. *J. Geophys. Res.*, in press.
- 755 Fu, Q., and K. N. Liou, 1993: Parameterization of the radiative properties of clouds. *J.*
756 *Atmos. Sci.*, **50**, 2008-2025.
- 757 Hallett, J., and S. C. Mossop, 1974: Production of secondary particles during the riming
758 process. *Nature*, **249**, 26-28.
- 759 Harrington, J., and P. Q. Olsson, 2001: On the potential influence of ice nuclei on
760 surface-forced marine stratocumulus cloud dynamics. *J. Geophys. Res.*, **106**(D21),
761 27473-27486, 10.1029/2000JD000236.
- 762 Harrington, J., and J. Verlinde, 2004: Mixed-phase Arctic Clouds Experiment (M-
763 PACE): The ARM scientific overview document, report, 20pp., U.S. Dep. of
764 Energy, Washington, D. C.
- 765 Harrington, J. Y., T. Reisin, W. R. Cotton, and S. M. Kreidenweis, 1999: Cloud resolving
766 simulations of Arctic stratus. Part II: Transition-season clouds. *Atmos. Res.*, **55**,
767 45-75.
- 768 Hobbs, P. V., 1969: Ice multiplication in clouds. *J. Atmos. Sci.*, **26**, 315-318.
- 769 Hobbs, P. V., and A. L. Rangno, 1998: Microstructure of low and middle-level clouds
770 over the Beaufort Sea. *Q. J. R. Meteor. Soc.*, **124**, 2035-2071.

- 771 Intrieri, J. M., M. D. Shupe, T. Uttal, and B. J. McCarty, 2002: An annual cycle of Arctic
772 cloud characteristics observed by radar and lidar at SHEBA. *J. Geophys. Res.*,
773 **107**, 8029, doi:10.1029/2000JC000423.
- 774 Jiang, H., W. R. Cotton, J. O. Pinto, J. A. Curry, and M. J. Weissbluth, 2000: Cloud
775 resolving simulations of mixed-phase Arctic stratus observed during BASE:
776 Sensitivity to concentration of ice crystals and large-scale heat and moisture
777 advection. *J. Atmos. Sci.*, **57**, 2105-2117.
- 778 Kattsov, V. M., and E. Kallen, 2004: Future climate change: Modeling and scenarios for
779 the Arctic. *Impacts of a Warming Arctic: Arctic Climate Impacts Assessment*, J. S.
780 Hassoll, Ed., Cambridge University Press, 99-150. [Available online at
781 www.acia.uaf.edu]
- 782 Klein, S., A. Fridlind, R. McCoy, G. McFarquhar, S. Menon, H. Morrison, S. Xie, J. J.
783 Yio, and M. Zhang, 2006: Arm Cloud Parameterization and Modeling Working
784 Group – GCSS Polar Cloud Working Group model intercomparison. Procedures
785 for ARM CPMWG Case 5/GCSS Polar Cloud WG SCM/CRM/LES
786 Intercomparison Case f2004: ARM Mixed-phase Arctic Cloud Experiment (M-
787 PACE): October 5-22, 2004. Available at
788 <http://science.arm.gov/workinggroup/cpm/scm/scmic5/index.html>.
- 789 Klein, S., and Coauthors, 2007: Intercomparison of model simulations of mixed-phase
790 clouds observed during the ARM Mixed-Phase Arctic Cloud Experiment, Part I:
791 Single-layered cloud, to be submitted to *Mon. Wea. Rev.*
- 792 Krueger, S. K., 1988: Numerical simulation of tropical cumulus clouds and their
793 interaction with the subcloud layer. *J. Atmos. Sci.*, **45**, 2221-2250.

- 794 Luo, Y., K.-M. Xu, H. Morrison, and G. McFarquhar, 2007a: Arctic mixed-phase clouds
795 simulated by a cloud-resolving model: Comparison with ARM observations and
796 sensitivity to microphysics parameterizations. *J. Atmos. Sci.*, in press.
- 797 Luo, Y., K.-M. Xu, B. A. Wielicki, Z. A. Eitzen, and T. Wong, 2007b: Statistical
798 analyses of satellite cloud object data from CERES. Part III: Comparison with
799 cloud-resolving model simulations of tropical convective clouds. *J. Atmos. Sci.*,
800 **64**, 762-785.
- 801 McFarquhar, G. M., and S. G. Cober, 2004: Single-scattering properties of mixed-phase
802 Arctic clouds at solar wavelengths: impacts on radiative transfer. *J. Climate*, **17**,
803 3799-3813.
- 804 McFarquhar, G. M., G. Zhang, M. Poellot, J. Verlinde, G. Kok, R. McCoy, T. Tooman,
805 and A. J. Heymsfield, 2007: Ice properties of single-layer stratocumulus during
806 the Mixed-Phase Arctic Cloud Experiment (M-PACE): Part I, Observations. *J.*
807 *Geophys. Res.*, in press.
- 808 Meyers, M. P., P. J. DeMott, and W. R. Cotton, 1992: New primary ice nucleation
809 parameterization in an explicit model. *J. Appl. Meteor.*, **31**, 708-721.
- 810 Morrison, H., and J. O. Pinto, 2006: Intercomparison of bulk cloud microphysics schemes
811 in mesoscale simulations of springtime Arctic mixed-phase stratiform clouds.
812 *Mon. Wea. Rev.*, **134**, 1880-1900.
- 813 Morrison, H., J. A. Curry, and V. I. Khvorostyanov, 2005: A new double-moment
814 microphysics parameterization for application in cloud and climate models. Part I:
815 Description. *J. Atmos. Sci.*, **62**, 1665-1677.

- 816 Morrison, H., J. O. Pinto, J. A. Curry, and G. M. McFarquhar, 2007a: Sensitivity of M-
817 PACE mixed-phase stratocumulus to cloud condensation and ice nuclei in a
818 mesoscale model with two-moment bulk cloud microphysics. *J. Geophys. Res.*, in
819 press.
- 820 Morrison, H., and Coauthors, 2007b: Intercomparison of model simulations of mixed-
821 phase clouds observed during the ARM Mixed-Phase Arctic Cloud Experiment,
822 Part II: Multi-layered cloud, to be submitted to *Mon. Wea. Rev.*
- 823 Pinto, J. O., 1998: Autumnal mixed-phase cloudy boundary layers in the Arctic. *J. Atmos.*
824 *Sci.*, **55**, 2016-2038.
- 825 Prenni, A. J., J. Y. Harrington, M. Tjernström, P. J. DeMott, A. Avramov, C. N. Long, S.
826 M. Kreidenweis, P. Q. Olsson, and J. Verlinde, 2007: Can ice-nucleating aerosols
827 affect Arctic seasonal climate? *Bull. Amer. Meteorol. Soc.*, in press.
- 828 Rangno, A. L., and P. V. Hobbs, 2001: Ice particles in stratiform clouds in the Arctic and
829 possible mechanisms for the production of high ice concentrations. *J. Geophys.*
830 *Res.*, **106**, 15,065-15,075.
- 831 Rogers, D. C., P. J. DeMott, S. M. Kreidenweis, and Y. Chen, 2001: A continuous-flow
832 diffusion chamber for airborne measurements of ice nuclei. *J. Atmos. Ocean.*
833 *Technol.*, **18**, 725-741.
- 834 Shupe, M. D., S. Y. Matrosov, and T. Uttal, 2005: Arctic mixed-phase cloud properties
835 derived from surface-based sensors. *Proc. 15th ARM Science Team Meeting*,
836 Daytona Beach, FL. Available from [http://www.arm.gov/publications](http://www.arm.gov/publications/proceedings/conf15/extended_abs/shupe_md.pdf)
837 [/proceedings /conf15/extended_abs/shupe_md.pdf](http://www.arm.gov/publications/proceedings/conf15/extended_abs/shupe_md.pdf)

- 838 Stokes, G. M., and S. E. Schwartz, 1994: The Atmospheric Radiation Measurement
839 (ARM) Program: Programmatic background and design of the Cloud and
840 Radiation Test Bed. *Bull. Amer. Meteor. Soc.*, **75**, 1201-1221.
- 841 Turner, D. D., S. A. Clough, J. C. Liljegren, E. E. Clothiaux, K. Cady-Pereira, and K. L.
842 Gaustad, 2007: Retrieving liquid water path and precipitable water vapor from
843 Atmospheric Radiation Measurement (ARM) microwave radiometers. *IEEE*
844 *Trans. Geosci. Remote Sens.*, submitted.
- 845 Uttal, T., and Coauthors, 2002: The surface heat budget of the Arctic Ocean. *Bull. Amer.*
846 *Meteor. Soc.*, **83**, 255-275.
- 847 Vavrus, S., 2004: The impact of cloud feedbacks on Arctic climate undergoing
848 greenhouse forcing. *J. Climate*, **17**, 603-615.
- 849 Wang, Z., and K. Sassen, 2001: Cloud type and macrophysical property retrieval using
850 multiple remote sensors. *J. Appl. Meteor.*, **40**, 1665-1682.
- 851 Wang, Z., K. Sassen, D. Whiteman, and B. Demoz, 2005: The analysis of multi-year low-
852 level and multi-level mixed-phase clouds observed at the North Slope of Alaska
853 Cloud and Radiation Testbed site. *Proc. 15th ARM Science Team Meeting*,
854 Daytona Beach, FL. Available from [http://www.arm.gov/publications](http://www.arm.gov/publications/proceedings/conf15/extended_abs/wang_z.pdf)
855 [/proceedings /conf15/extended_abs/wang_z.pdf](http://www.arm.gov/publications/proceedings/conf15/extended_abs/wang_z.pdf)
- 856 Verlinde, J., and coauthors, 2007: The Mixed-Phase Arctic Cloud Experiment (M-
857 PACE). *Bull. Amer. Met. Soc.*, **88**, 205-221.
- 858 Xie, S., S. A. Klein, M. Zhang, J. J. Yio, R. T. Cederwall, and R. McCoy, 2006:
859 Developing large-scale forcing data for single-column and cloud-resolving

860 models from the Mixed-Phase Arctic Cloud Experiment. *J. Geophys. Res.*, **111**,
861 D19104, doi:10.1029/2005JD006950.

862 Xu, K.-M., and S. K. Krueger, 1991: Evaluation of cloudiness parameterizations using a
863 cumulus ensemble model. *Mon. Wea. Rev.*, 119, 342-367.

864 Xu, K.-M., and D. A. Randall, 1995: Impact of interactive radiative transfer on the
865 macroscopic behavior of cumulus ensembles. Part I: Radiation parameterization
866 and sensitivity tests. *J. Atmos. Sci.*, 52, 785-799.

867 Xu, K.-M., and coauthors, 2005: Modeling springtime shallow frontal clouds with cloud-
868 resolving and single-column models. *J. Geophys. Res.*, 110, D15S04, doi:
869 10.1029/2004JD005153.

870 Zhang, M. H., and J. L. Lin, 1997: Constrained variational analysis of sounding data
871 based on column-integrated budgets of mass, heat, moisture, and momentum:
872 Approach and application to ARM measurements. *J. Atmos. Sci.*, **54**, 1503-1524.

873 Zhang, M. H., J. L. Lin, R. T. Cederwall, J. J. Yio, and S. C. Xie, 2001: Objective
874 analysis of ARM IOP data: Method and sensitivity. *Mon. Wea. Rev.*, **129**, 295-
875 311.

876

876 Table 1. A list of simulations performed in this study. See text for further explanations.

<i>Simulation</i>	<i>Description</i>
Baseline	Standard baseline simulation
noLSforcing	Neglecting large-scale advective forcing
noSfcFlx	Neglecting surface turbulent fluxes of latent and sensible heat
noLWrad	Neglecting longwave radiative cooling/heating
noIce	Neglecting ice-phase microphysical processes
noMicLat	Neglecting cooling/heating caused by phase change of hydrometeors

877

878

879 Table 2. Occurrences of single-layer, double-layer, and three-layer mixed-phase clouds,
 880 respectively, based on the MMCR-MPL measurements and from the Baseline simulation
 881 by the CRM. Values outside of brackets are the numbers of occurrence and values inside
 882 brackets are the relative frequencies of occurrence of these cloud layers.

	<i>1-layer</i>	<i>2-layer</i>	<i>3-layer</i>
MMCR-MPL 10/06	1186 [49%]	997 [41%]	206 [9%]
MMCR-MPL 10/07	1532 [66%]	721 [31%]	70 [3%]
MMCR-MPL 10/08	2010 [90%]	225 [10%]	8 [0%]
MMCR-MPL 10/06-10/08	4728 [68%]	1943 [28%]	284 [4%]
CRM 12-36 h	10574 [29%]	23825 [64%]	2584 [7%]
CRM 36-60 h	13137 [63%]	7574 [36%]	139 [1%]
CRM 60-84 h	23584 [66%]	12381 [34%]	9 [0%]
CRM 12-84 h	47295 [50%]	43780 [47%]	2732 [3%]

883

884

885

886

887

887 Table 3. The T-statistic (T) and its significance (P) for liquid water content (LWC), cloud
888 droplet number concentration (n_c), ice plus snow water content (ISWC), and ice crystal
889 number concentration (n_{is}) during the three subperiods A, B, and C.

890

subperiod	LWC		n_c		ISWC		n_{is}	
	T	P	T	P	T	P	T	P
A	7.12	0.00	5.79	0.00	-26.37	0.00	-32.19	0.00
B	1.36	0.18	-5.68	0.00	-13.39	0.00	-30.75	0.00
C	3.68	0.00	42.17	0.00	-16.25	0.00	-34.68	0.00

891

892

Figure Captions

892

893

894 Figure 1. The area of the M-PACE campaign. Asterisks are the locations of the sounding
895 stations. Sounding data are used to derive large-scale forcing data over the area enclosed
896 by dashed lines. The latitudes and longitudes are represented by dotted lines and the solid
897 line represents the coastline.

898

899 Figure 2. Profiles of the sample numbers for liquid water content (solid lines) and ice
900 water content (dashed lines), respectively, in each height bin of 400 m during the three
901 missions that the UND Citation took on October 5 (a), October 6 (b), and October 8 (c),
902 2004.

903

904 Figure 3. The large-scale forcing data used to drive the CRM. Panels (a) and (b) represent
905 the time-pressure cross sections of the large-scale advective tendencies of temperature
906 and water vapor mixing ratio, respectively. The hatched areas in panel (a) represent
907 warming (cooling) rates larger than 4 K day^{-1} and in panel (b) represent moistening
908 (drying) rates larger than $2 \text{ g kg}^{-1} \text{ day}^{-1}$. Panel (c) represents the time-series of the surface
909 turbulent fluxes of latent heat (solid line) and sensible heat (dashed line) with the labels
910 “A”, “B” and “C” indicating the periods of the Citation missions taken on October 5, 6,
911 and 8, respectively. Panel (d) shows the spectral albedo over fresh snow corresponding to
912 a broadband albedo of 0.86 for the six shortwave bands of the Fu and Liou (1993)
913 radiative transfer scheme.

914

915 Figure 4. Time-pressure cross sections of temperature (a) and water vapor mixing ratio
916 (b) from the Baseline simulation, and the differences from the ARM analysis in
917 temperature (c) and water vapor mixing ratio (d). Panel (e) shows the time-series of
918 surface precipitation rate from the M-PACE observations (solid line) and the Baseline
919 simulation (dashed line).

920

921 Figure 5. Time-height cross section of 3-hourly and horizontally averaged (a) liquid
922 water content (color shades) and ice plus snow water content (lines) (unit: g m^{-3}), (b) LW
923 radiative cooling (negative) rates, and (c) heating rates caused by microphysical
924 processes from the Baseline simulation. The unit of the color bars in (b) and (c) is K day^{-1} .
925

926 Figure 6. Histograms of base height (a and d), top height (b and e), and physical thickness
927 (c and f) of the first mixed-phase cloud layer above the surface from the Baseline
928 simulation (left column) and the MMCR-MPL observations at Barrow (right column).
929

929

930 Figure 7. Same as Figure 6 except for the second mixed-phase cloud layer above the
931 surface.

932

933 Figure 8. Time series of 3-hourly averaged liquid water path produced by the Baseline
934 simulation averaged over the CRM domain (line without symbols) and derived from the
935 microwave radiometer measurements at the DOE-ARM NSA sites (line with crosses).
936

936

937 Figure 9. Vertical profiles of liquid water content from the Baseline simulation during 12-
938 24 h (a), 24-36 h (b), and 72-84 h (c) and from the Citation measurements taken on
939 October 5 (d), October 6 (e), and October 8 (f). The solid lines represent the means and
940 the shades represent plus and minus one standard deviation from the means.

941

942 Figure 10. Same as Figure 9 except for droplet number concentration.

943

944 Figure 11. Same as Figure 9 except for total ice water content.

945

946 Figure 12. Same as Figure 9 except for ice crystal number concentration.

947

948 Figure 13. Time-height cross sections of 3-hourly and horizontally-averaged liquid water
949 content (color shades) and ice plus snow water content (lines) from the noSfcFlx (a),
950 noLSadv (b), noLWrad (c), noIce (d), and noMicLat (e) experiments. See the text for
951 further explanations about the experiments.

952

953 Figure 14. Profiles of the differences in horizontally averaged potential temperature (a)
954 and water vapor mixing ratio (b) between the Baseline simulation and the noSfcFlx
955 experiment. The six lines in each panel represent the results averaged over the six 12 h
956 subperiods: solid lines for 12-24 h, long dashed lines for 24-36 h, dots-dashed lines for
957 36-48 h, dot-dashed lines for 48-60 h, short dashed lines for 60-72 h, and dotted lines for
958 72-84 h.

959

960 Figure 15. Vertical profiles of the horizontally averaged resolved-scale kinetic energy in
961 the CRM simulations. Lines with stars represent the means over 12-84 h and shades
962 represent plus and minus one standard deviation from the means.

963

964 Figure 16. Same as Figure 15 except for the turbulent kinetic energy (TKE).

965

965
966
967
968
969
970
971
972
973
974
975
976
977
978
979
980
981
982
983
984
985
986
987
988
989
990
991
992
993
994
995
996
997
998
999
1000
1001

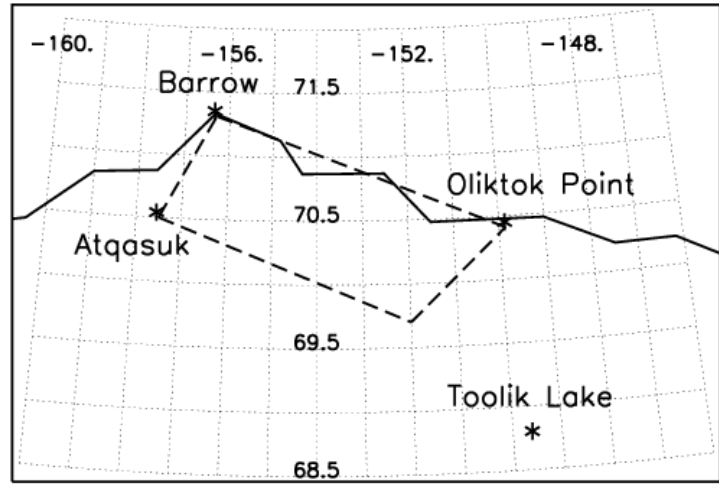
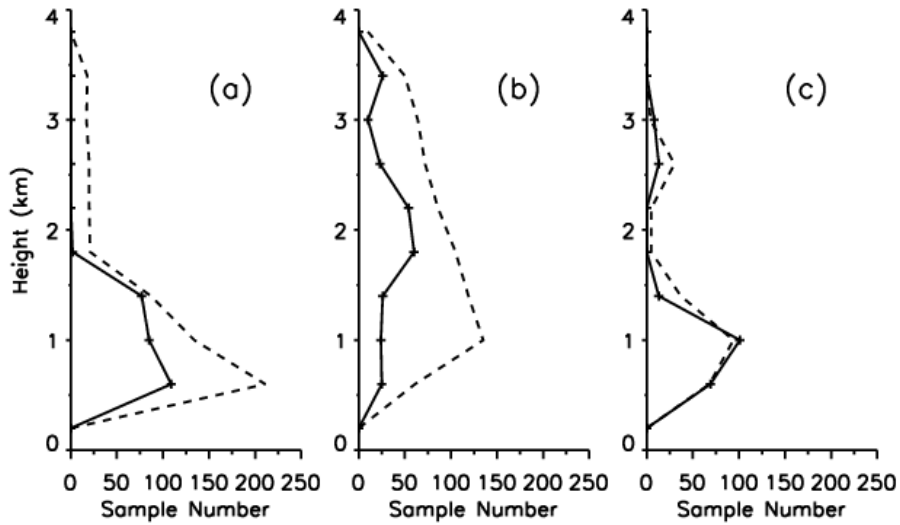


Figure 1. The area of the M-PACE campaign. Asterisks are the locations of the sounding stations. Sounding data are used to derive large-scale forcing data over the area enclosed by dashed lines. The latitudes and longitudes are represented by dotted lines and the solid line represents the coastline.



1001
1002
1003
1004
1005
1006
1007
1008
1009
1010
1011
1012
1013
1014
1015
1016
1017
1018
1019
1020
1021
1022
1023
1024
1025
1026
1027
1028
1029

Figure 2. Profiles of the sample numbers for liquid water content (solid lines) and ice water content (dashed lines), respectively, in each height bin of 400 m during the three missions that the UND Citation took on October 5 (a), October 6 (b), and October 8 (c), 2004.

1029
1030

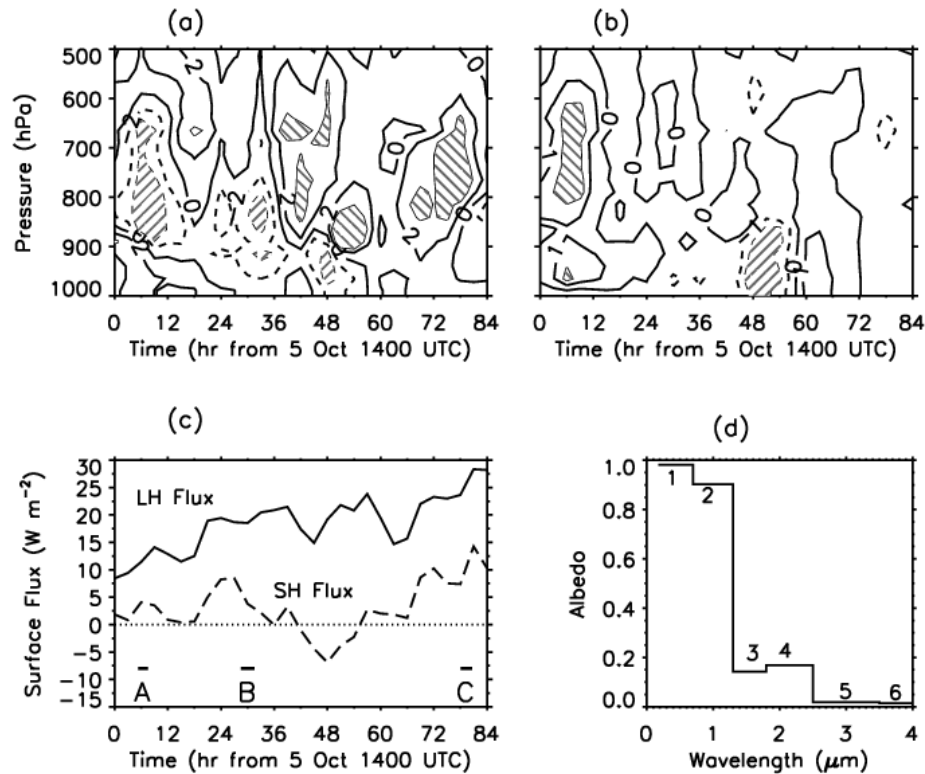


Figure 3. The large-scale forcing data used to drive the CRM. Panels (a) and (b) represent the time-pressure cross sections of the large-scale advective tendencies of temperature and water vapor mixing ratio, respectively. The hatched areas in panel (a) represent warming (cooling) rates larger than 4 K day^{-1} and in panel (b) represent moistening (drying) rates larger than $2 \text{ g kg}^{-1} \text{ day}^{-1}$. Panel (c) represents the time-series of the surface turbulent fluxes of latent heat (solid line) and sensible heat (dashed line) with the labels “A”, “B” and “C” indicating the periods of the Citation missions taken on October 5, 6, and 8, respectively. Panel (d) shows the spectral albedo over fresh snow corresponding to a broadband albedo of 0.86 for the six shortwave bands of the Fu and Liou (1993) radiative transfer scheme.

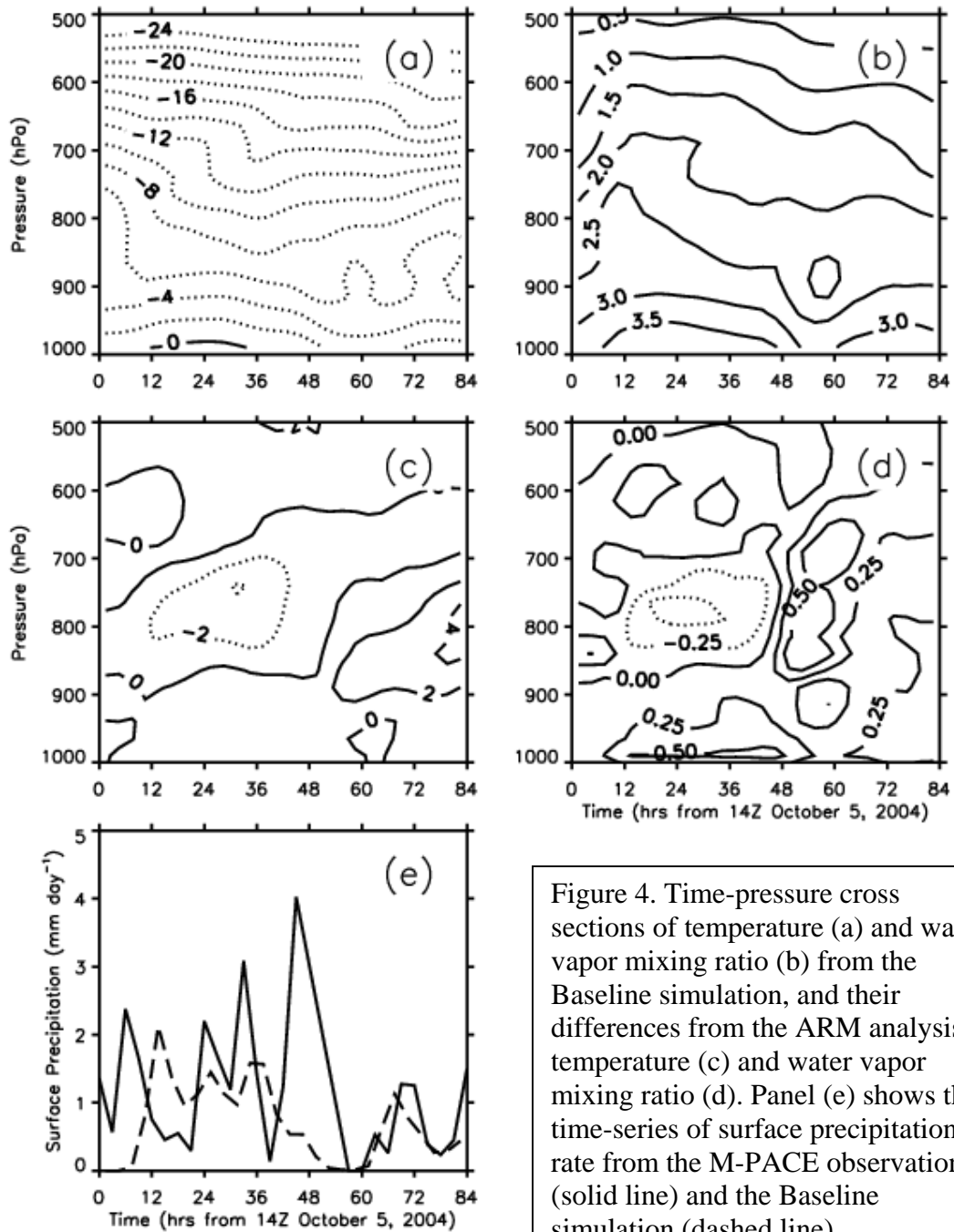
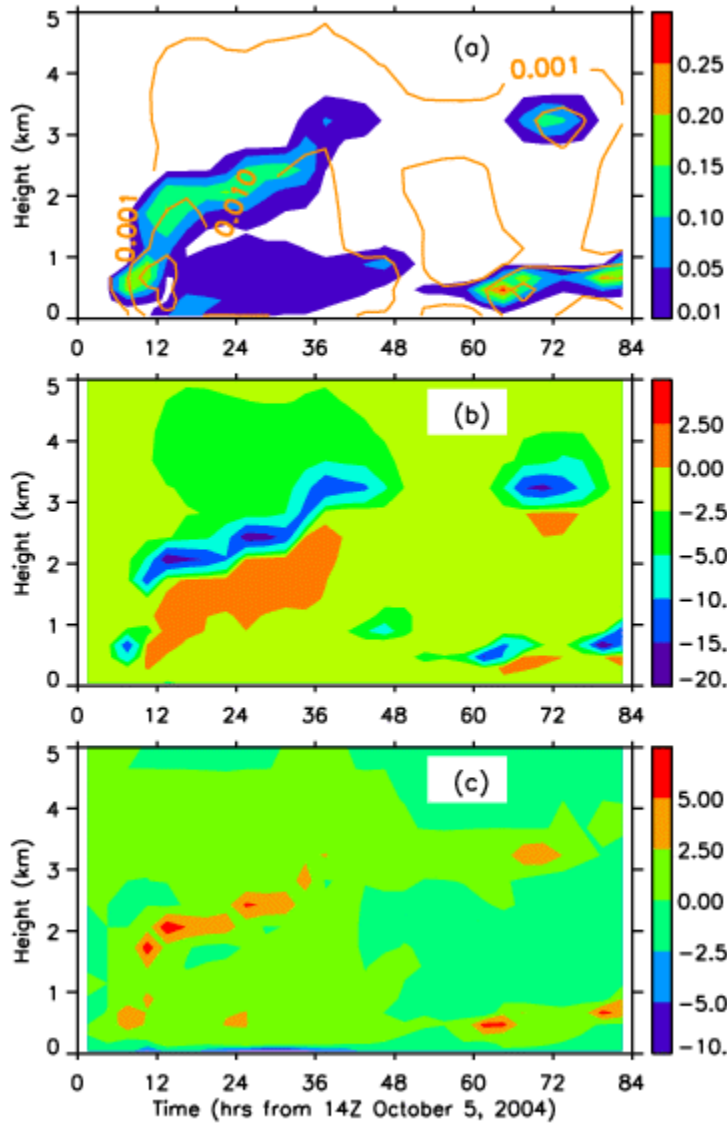


Figure 4. Time-pressure cross sections of temperature (a) and water vapor mixing ratio (b) from the Baseline simulation, and their differences from the ARM analysis in temperature (c) and water vapor mixing ratio (d). Panel (e) shows the time-series of surface precipitation rate from the M-PACE observations (solid line) and the Baseline simulation (dashed line).



1031
1032
1033
1034
1035

Figure 5. Time-height cross section of 3-hourly and horizontally averaged (a) liquid water content (color shades) and ice plus snow water content (lines) (unit: g m^{-3}), (b) LW radiative cooling (negative) rates, and (c) heating rates caused by microphysical processes from the Baseline simulation. The unit of the color bars in (b) and (c) is K day^{-1} .

1035
1036
1037
1038
1039
1040
1041
1042
1043
1044
1045
1046
1047
1048
1049
1050
1051
1052
1053
1054
1055
1056
1057
1058
1059
1060
1061
1062
1063
1064
1065
1066
1067
1068
1069
1070
1071
1072
1073

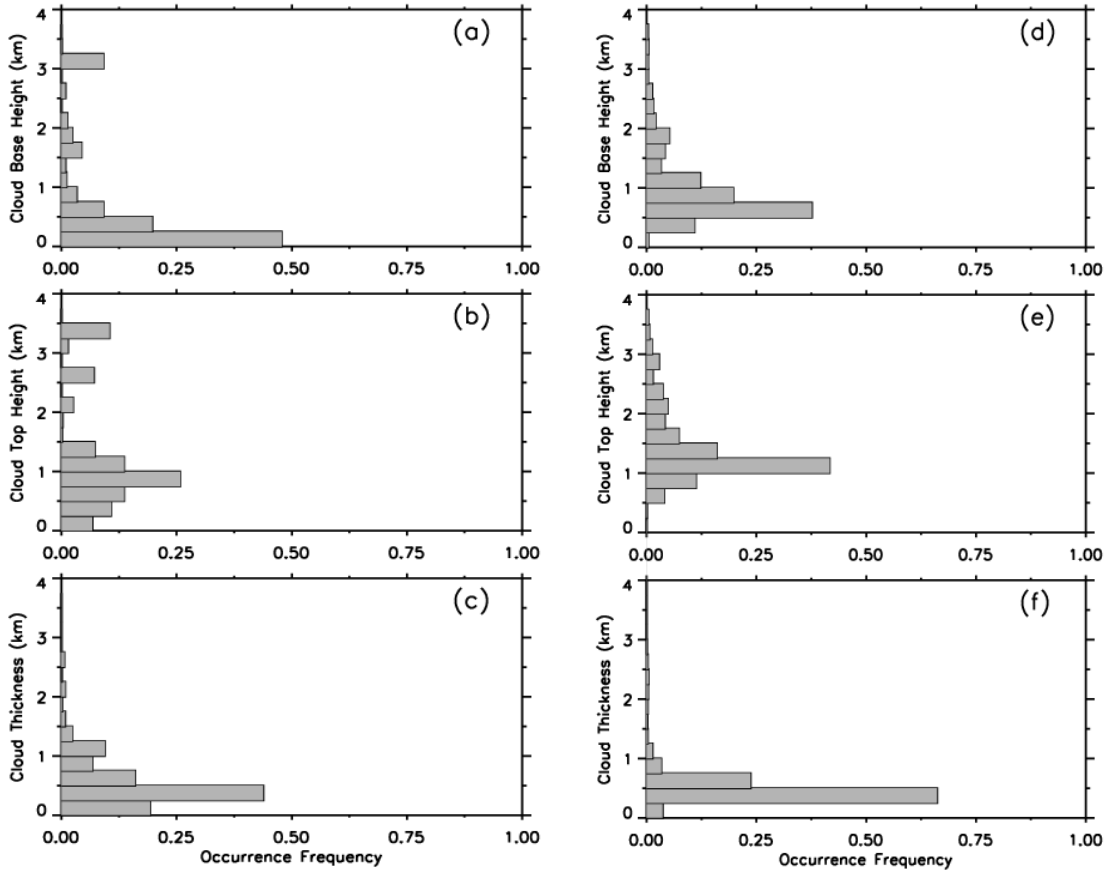


Figure 6. Histograms of base height (a and d), top height (b and e), and physical thickness (c and f) of the first mixed-phase cloud layer above the surface from the Baseline simulation (left column) and the MMCR-MPL observations at Barrow (right column).

1073
1074
1075
1076
1077
1078
1079
1080
1081
1082
1083
1084
1085
1086
1087
1088
1089
1090
1091
1092
1093
1094
1095
1096
1097
1098
1099
1100
1101
1102

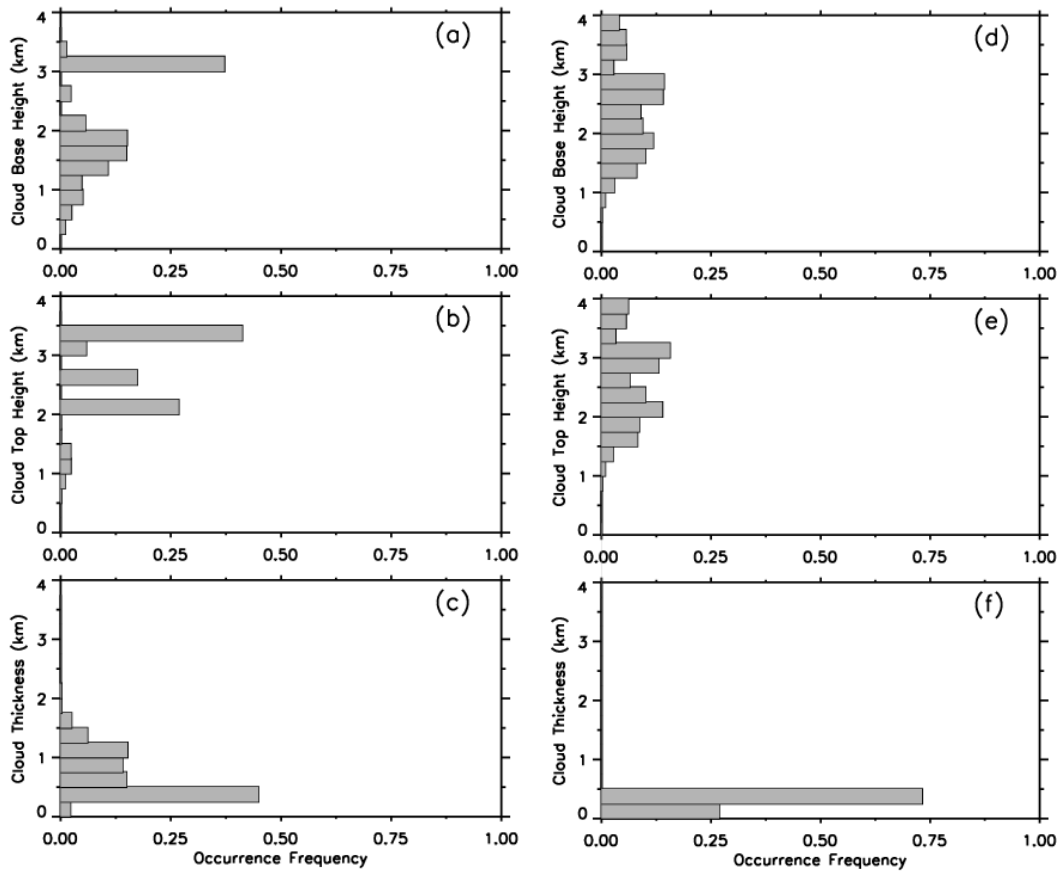


Figure 7. Similar to Figure 6 except for the second mixed-phase cloud layer above the surface.

1102

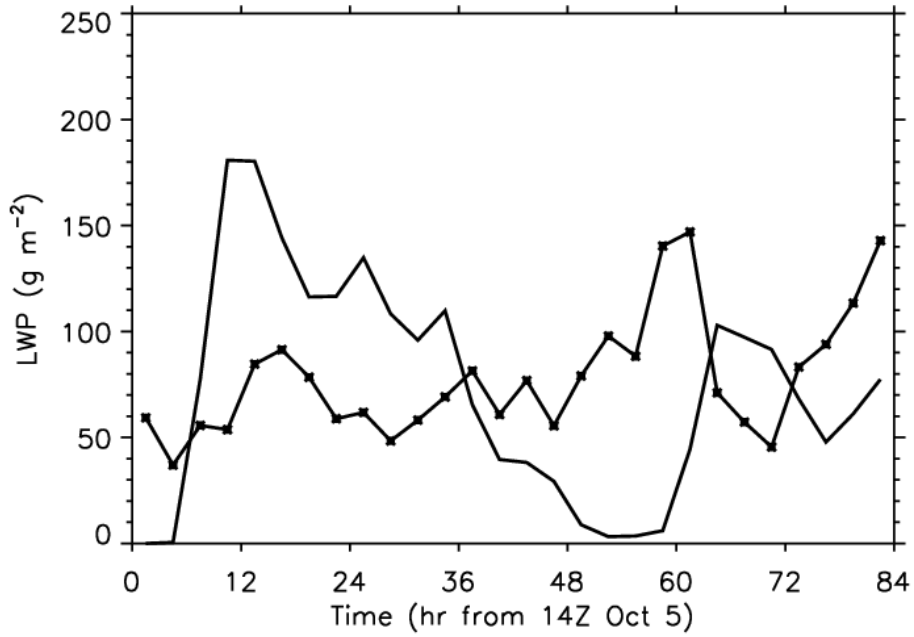


Figure 8. Time series of 3-hourly averaged liquid water path produced by the Baseline simulation averaged over the CRM domain (line without symbols) and derived from the microwave radiometer measurements at the DOE-ARM NSA sites (line with crosses).

1102
1103
1104
1105
1106
1107
1108
1109
1110
1111
1112
1113
1114
1115
1116
1117
1118
1119
1120
1121
1122
1123
1124
1125
1126
1127
1128
1129
1130
1131
1132
1133
1134
1135
1136
1137
1138
1139
1140
1141
1142
1143
1144
1145

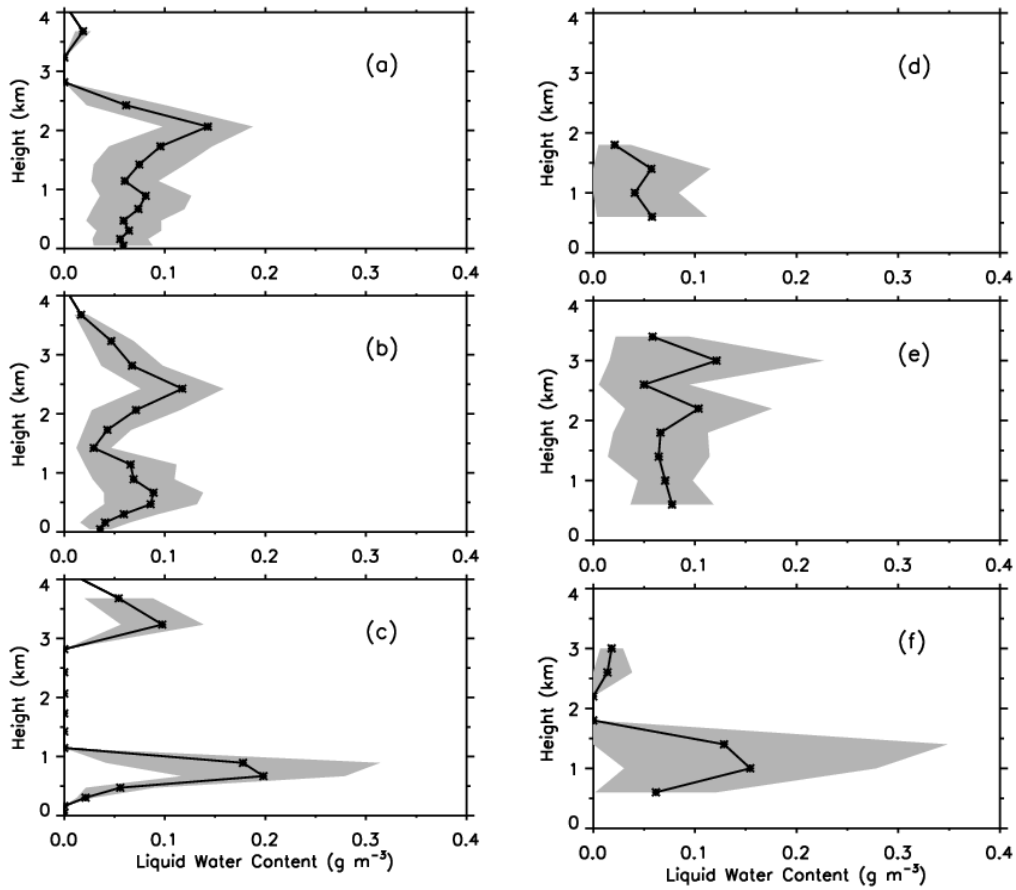


Figure 9. Vertical profiles of liquid water content from the Baseline simulation during 12-24 h (a), 24-36 h (b), and 72-84 h (c) and from the Citation measurements taken on October 5 (d), October 6 (e), and October 8 (f). The solid lines represent the means and the shades represent plus and minus one standard deviation from the means.

1145
1146
1147
1148
1149
1150
1151
1152
1153
1154
1155
1156
1157
1158
1159
1160
1161
1162
1163
1164
1165
1166
1167
1168
1169
1170
1171
1172
1173
1174
1175
1176
1177
1178
1179
1180
1181
1182
1183
1184

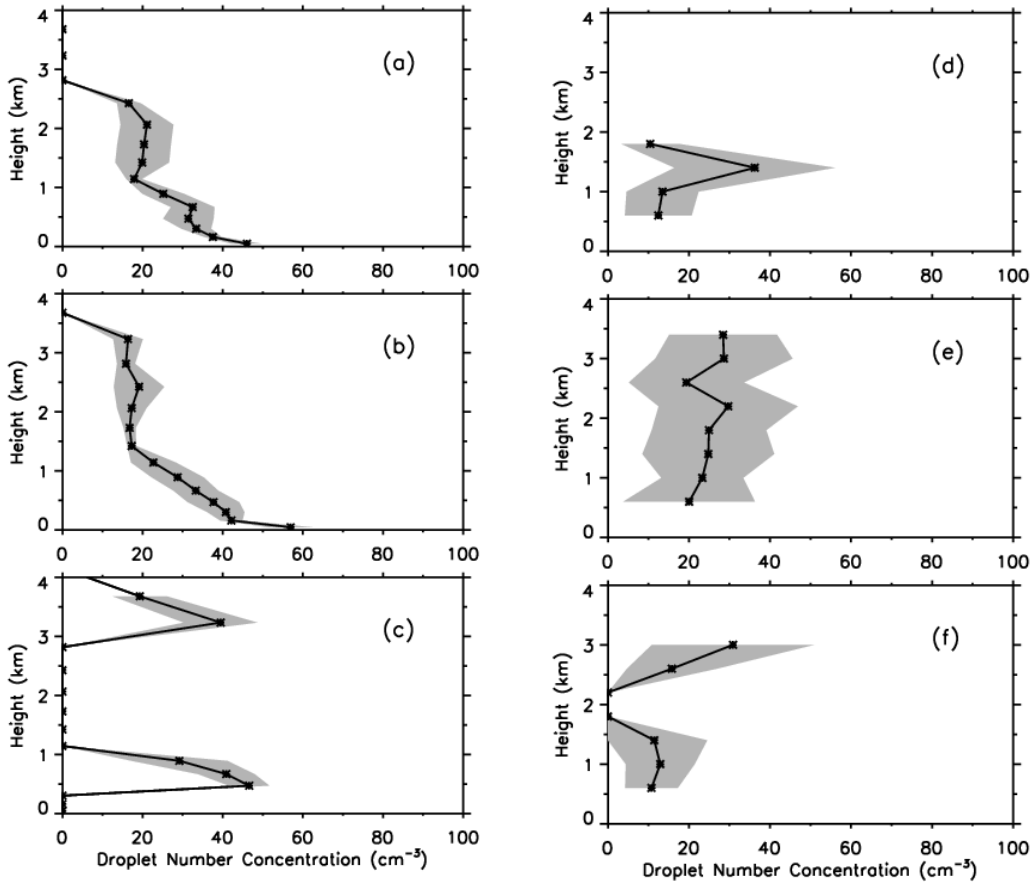


Figure 10. Same as Figure 9 except for droplet number concentration.

1184
1185
1186
1187
1188
1189
1190
1191
1192
1193
1194
1195
1196
1197
1198
1199
1200
1201
1202
1203
1204
1205
1206
1207
1208
1209
1210
1211
1212
1213
1214
1215
1216

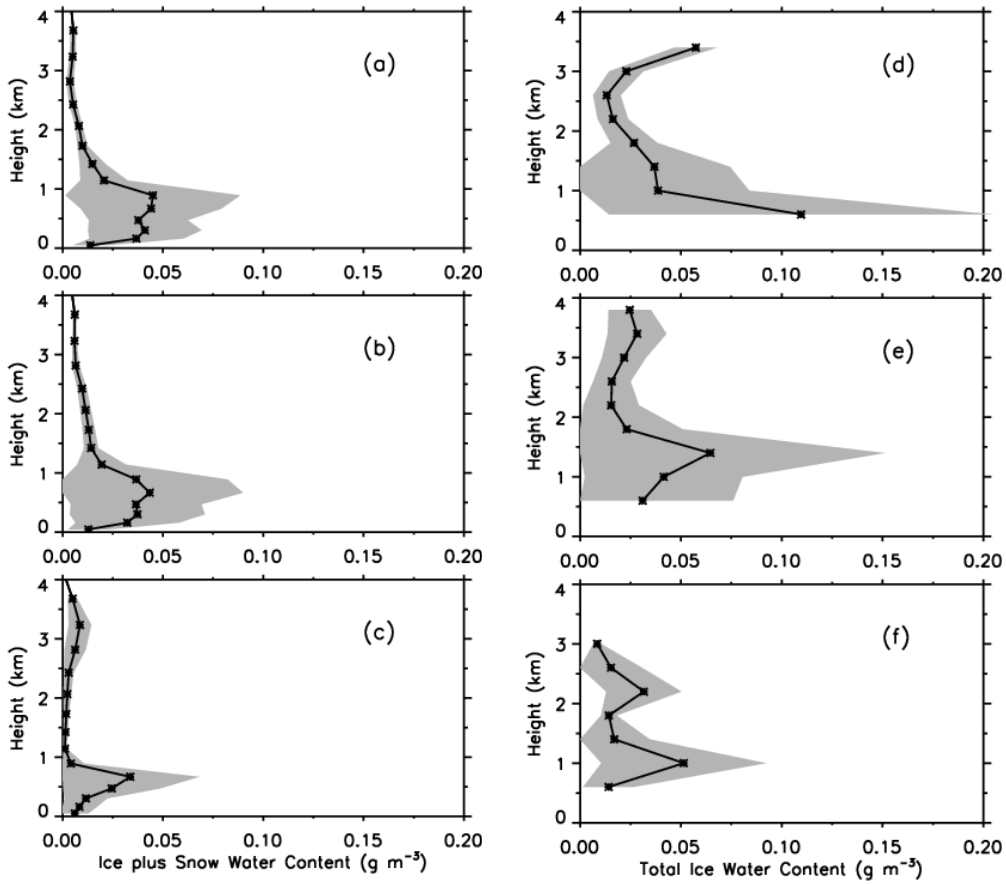


Figure 11. Same as Figure 9 except for total ice water content.

1216
1217
1218
1219
1220
1221
1222
1223
1224
1225
1226
1227
1228
1229
1230
1231
1232
1233
1234
1235
1236
1237
1238
1239
1240
1241
1242
1243
1244
1245
1246
1247
1248
1249
1250
1251
1252
1253
1254
1255
1256
1257
1258
1259
1260
1261

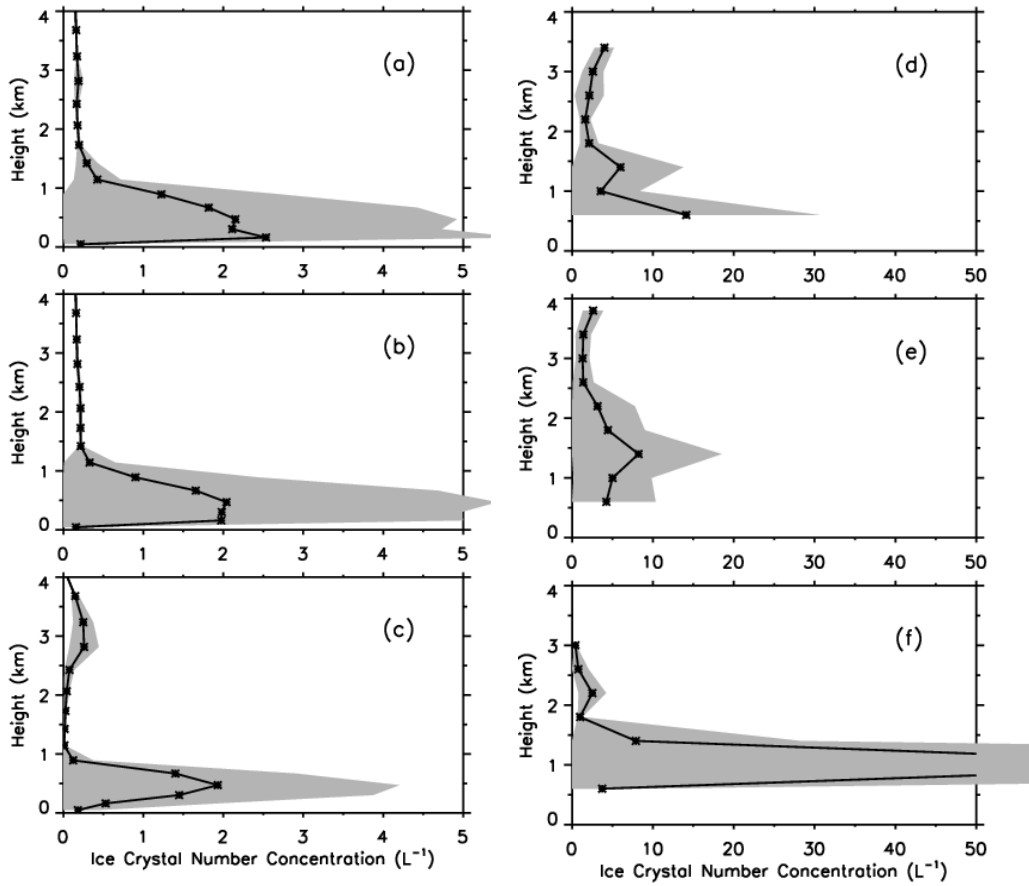
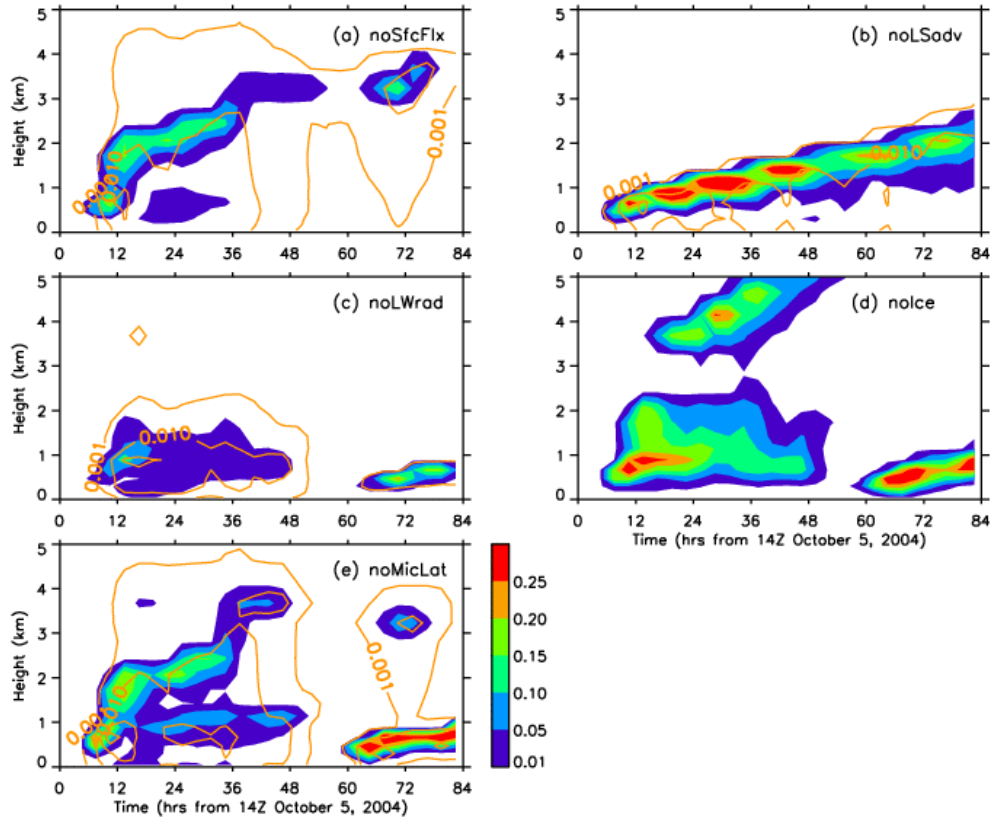


Figure 12. Same as Figure 9 except for ice crystal number concentration.

1261



1262
1263
1264
1265
1266
1267
1268
1269
1270
1271
1272
1273

Figure 13. Time-height cross sections of 3-hourly and horizontally-averaged liquid water content (color shades) and ice plus snow water content (lines) from the noSfcFlx (a), noLSadv (b), noLWrad (c), noIce (d), and noMicLat (e) experiments. See the text for further explanations about the experiments.

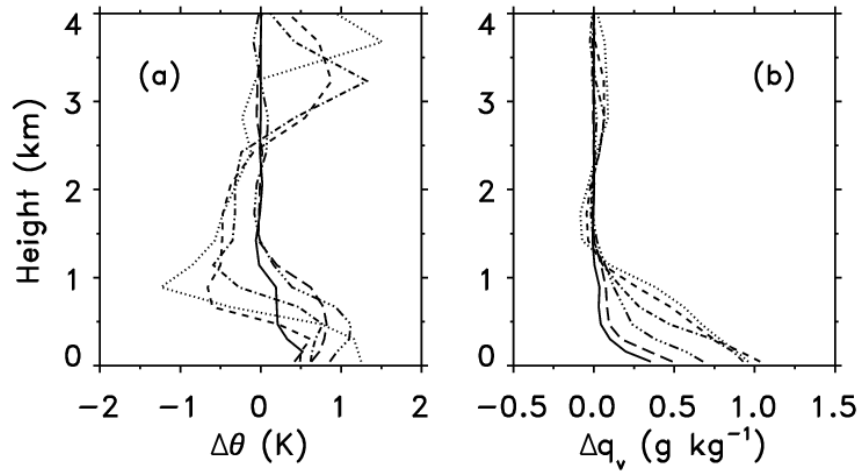
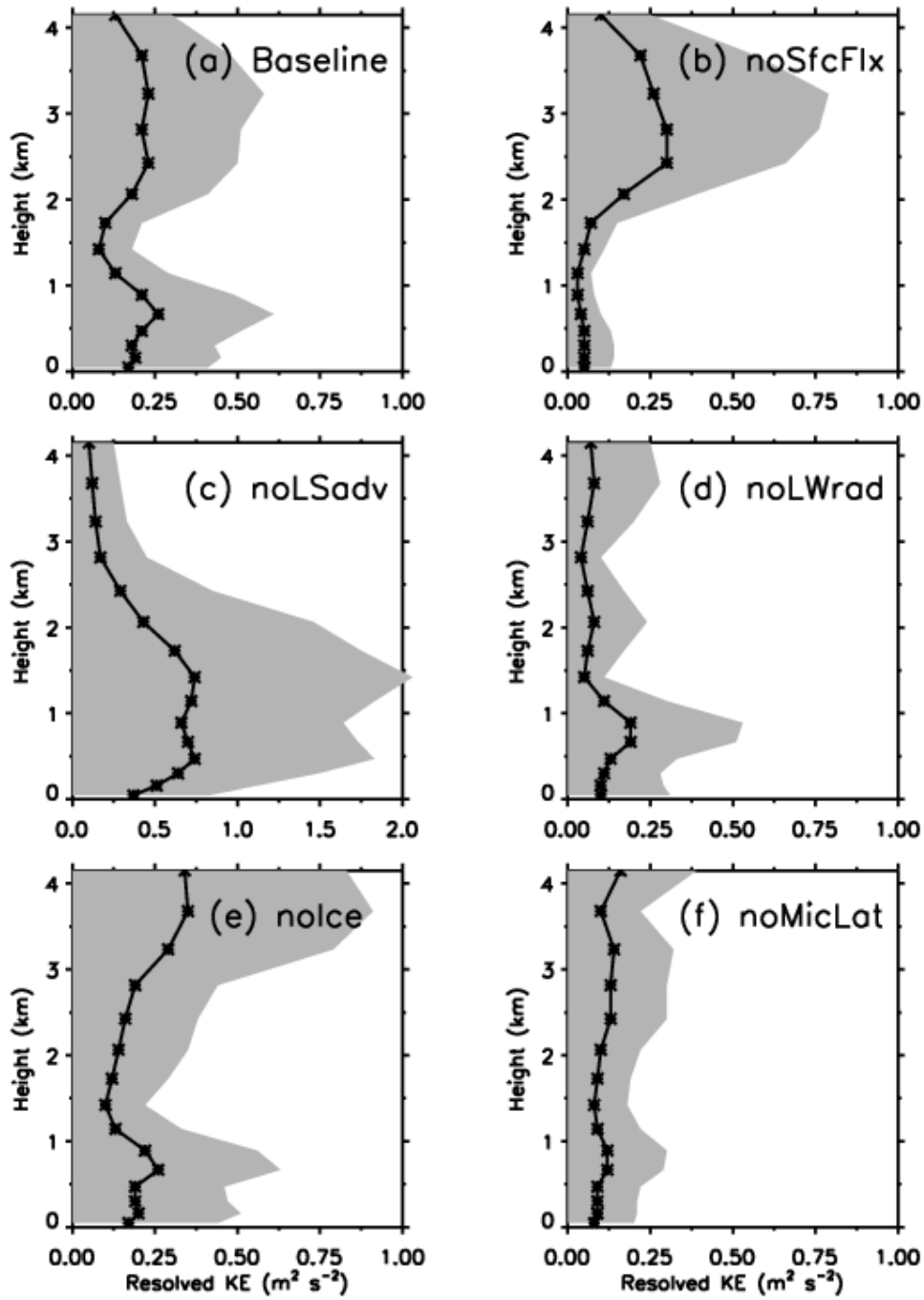
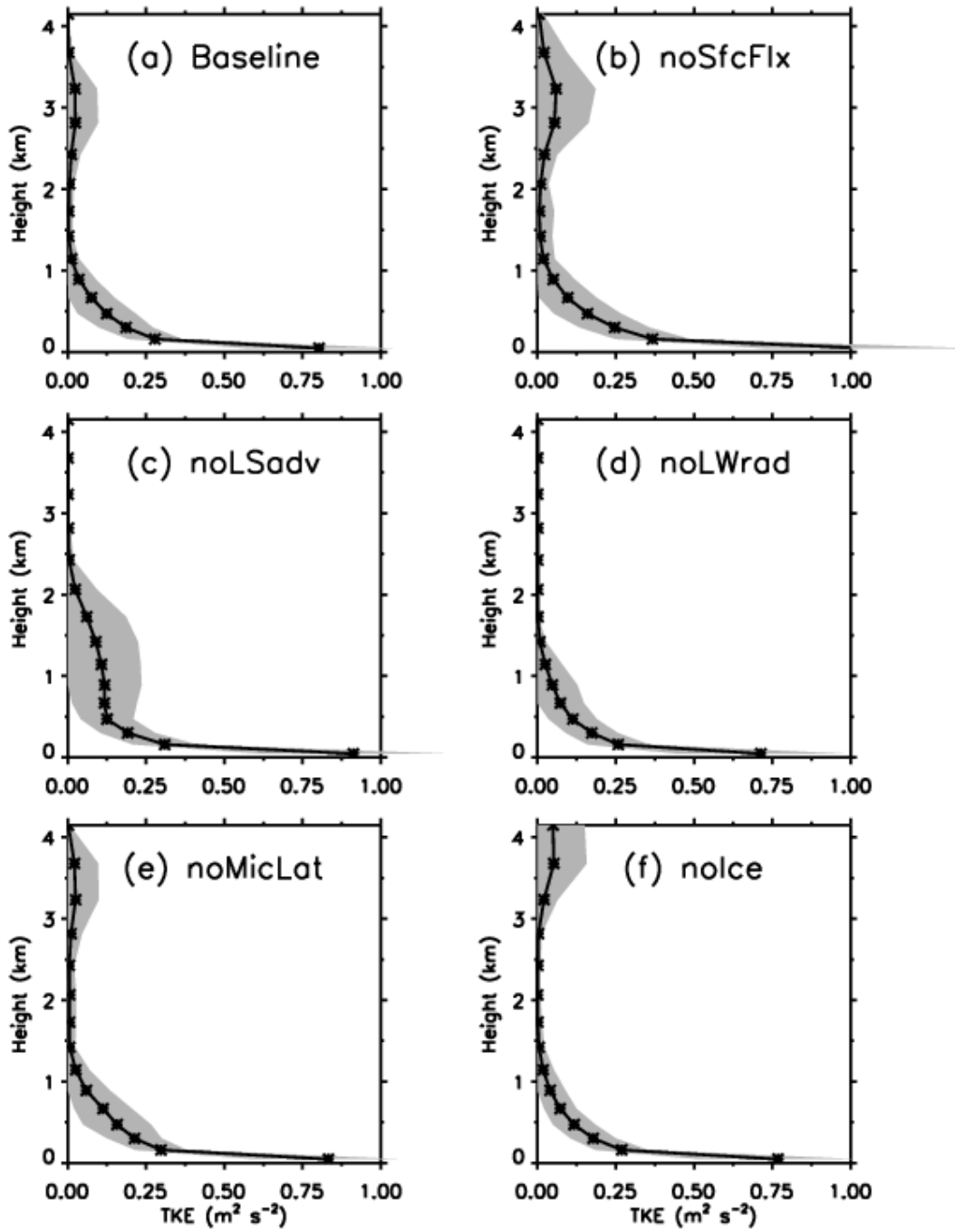


Figure 14. Profiles of the differences in horizontally averaged potential temperature (a) and water vapor mixing ratio (b) between the Baseline simulation and the noSfcFlx experiment. The six lines in each panel represent the results averaged over the six 12 h subperiods: solid lines for 12-24 h, long dashed lines for 24-36 h, dots-dashed lines for 36-48 h, dot-dashed lines for 48-60 h, short dashed lines for 60-72 h, and dotted lines for 72-84 h.



1318
1319
1320
1321
1322
1323
1324
1325

Figure 15. Vertical profiles of the horizontally averaged resolved-scale kinetic energy in the CRM simulations. Lines with stars represent the means over 12-84 h and shades represent plus and minus one standard deviation from the means.



1325
1326
1327
1328
1329
1330
1331

Figure 16. Same as Figure 15 except for the turbulent kinetic energy (TKE).